

Strong Electronic Metal–Support Interactions Enable the Increased Spin State of Co–N₄ Active Sites and Performance for Acidic Oxygen Reduction Reaction

Miao-Ying Chen,[#] Shuhu Yin,[#] Gen Li, Junxiang Chen, Wen-Yuan Zhao, Yi-Kai Lian, Hao-Ran Wu, Wenfu Yan, Jia-Nan Zhang,^{*} and Bang-An Lu^{*}



Cite This: *ACS Nano* 2024, 18, 26115–26126



Read Online

ACCESS |

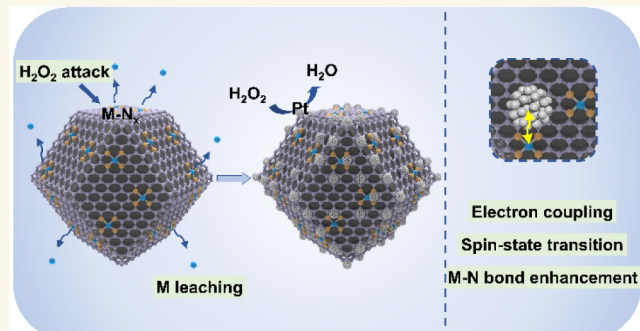
Metrics & More

Article Recommendations

Supporting Information

ABSTRACT: Nonprecious metal catalysts, particularly M–N–C catalysts, are widely recognized as promising contenders for the oxygen reduction reaction (ORR). However, a notable performance gap persists between M–N–C catalysts and Pt-based catalysts under acidic conditions. In this study, hybrid catalysts comprising single Co atoms and ultralow concentrations of Pt₃Co intermetallic nanoparticles (NPs) are introduced to enhance ORR performance. Under acidic conditions, these hybrid catalysts demonstrate ORR efficiency with a half-wave potential of 0.895 V, negligible decay even after 80 000 cycles, and a high maximum power density of 1.34 W cm⁻² in fuel cells. This performance surpasses those of Co–N–C and Pt/Co–N–C catalysts. Both experimental findings and theoretical computations suggest that the heightened ORR activity stems from an increase in the spin density of Co sites induced by noble metal NPs, facilitating the activation of O–O bonds *via* side-on overlapping and enabling a transition in the reaction pathway from associative to dissociative processes. This research offers a promising avenue for the systematic design of M–N–C cathodes with an enhanced performance for acidic fuel cells.

KEYWORDS: M–N–C catalysts, oxygen reduction reaction, multiple active centers, strong interaction between metal and support, durability



INTRODUCTION

The sluggish cathodic oxygen reduction reaction (ORR) demands a substantial amount of Pt catalyst, yet its limited availability and high cost pose significant hurdles for the widespread adoption of fuel cells.^{1–3} Decreasing Pt loading exacerbates oxygen transfer resistance due to constrained electrochemically active sites, leading to diminished durability.^{4–6} Conversely, non-noble metal nitrogen doped carbon material (M–N–C, M = Fe, Co, Mn, etc.) catalysts have emerged as promising nonplatinum catalysts, garnering considerable attention.^{7–13} However, their poor stability during proton exchange membrane fuel cell (PEMFC) operation remains a major impediment to industrial application.^{13–16} Previous studies have both theoretically and experimentally revealed that the metallic sites of M–N–C are prone to dissolution in acidic electrochemical environments, thereby compromising active sites, contaminating polymer

electrolytes, and generating corrosive radicals.^{17–21} There is an urgent need to develop efficient cathode catalysts that strike a balance between catalyst cost and the enduring stability requisite for practical fuel cell utilization.

According to recent research, the demetalation process in M–N–C catalysts can be efficiently impeded by a robust interaction with metallic particles, such as clusters and nanoparticles, rendering it one of the few promising strategies for enhancing stability.^{22–25} For instance, Shui *et al.*²³ demonstrated that the Fe clusters optimize the adsorption

Received: May 19, 2024

Revised: August 6, 2024

Accepted: August 7, 2024

Published: September 12, 2024



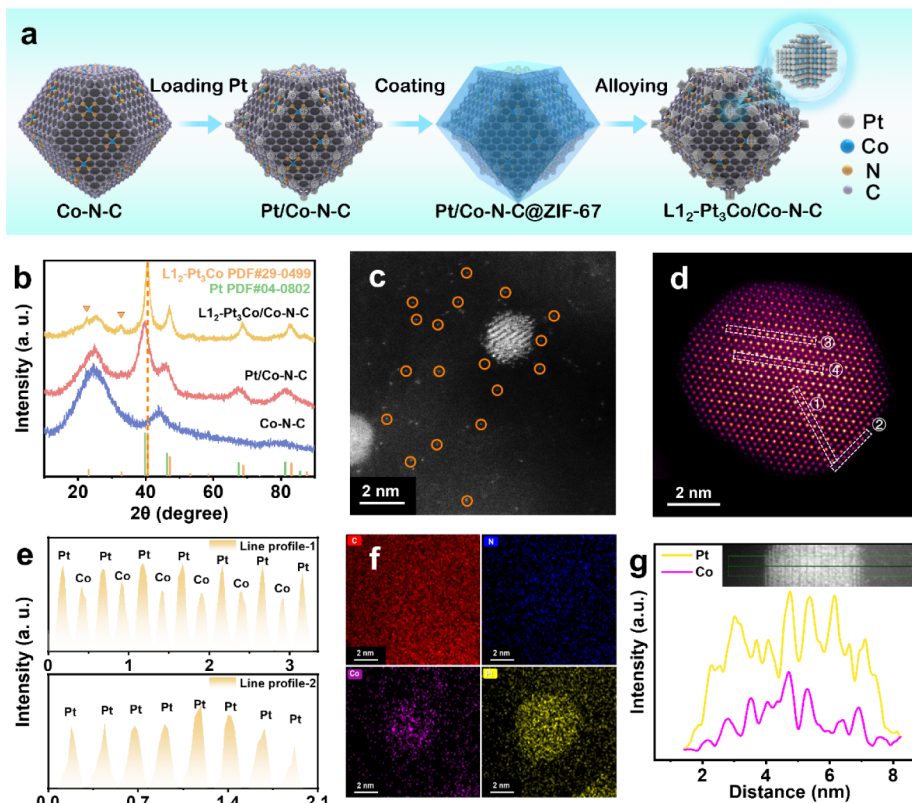


Figure 1. Morphology and structure of catalysts. (a) Preparation illustration of the L1₂-Pt₃Co/Co-N-C hybrid catalyst. (b) XRD patterns of Co-N-C, Pt/Co-N-C, and L1₂-Pt₃Co/Co-N-C. (c,d) AC-HAADF-STEM images of L1₂-Pt₃Co/Co-N-C. The orange circles represent the atomic Co sites. (e) Line scan profiles corresponding to the white box in (d). (f) EDS elemental mappings of C, N, Co, and Pt within L1₂-Pt₃Co/Co-N-C. (g) Elemental line-scanning of single L1₂-Pt₃Co NPs. Inset: Line-scanning direction of metal particles.

strength of oxygen reduction intermediates on Fe–N₄ while also reducing the bond amplitude of Fe–N₄ through incoherent vibrations. Furthermore, the application of Pt-based nanoparticles (NPs) has been demonstrated to improve the durability and activity of M–N–C catalysts.^{25–29} A hybrid catalyst with an ultralow Pt loading (2–3 wt %) was presented by Liu *et al.*,⁵ which was composed of Pt–Co alloy NPs supported on a Co–N–C framework. This catalyst exhibited an impressive ORR activity (1.77 A mg_{Pt}⁻¹ at 0.9 V_{iR-free}). Similarly, Shao *et al.*⁶ reported a Pt–Fe–N–C catalyst featuring Pt–Fe alloy NPs supported on Fe–N–C with a Pt loading of 1.7 wt %. Likewise, Sun's group³⁰ demonstrated that PtFe–FeNC exhibited high Pt mass activity (MA) of 1.75 A mg_{Pt}⁻¹ at 0.9 V_{iR-free} in fuel cells, with only a 12.5% decrease in peak power density compared to the 51.7% decrease observed with FeNC alone. Zheng *et al.*³¹ proposed that metal particles function as electron donors, reducing the Fe oxidation state by enhancing electron density at the MN₄ position, thereby fortifying the Fe–N bond and inhibiting electrochemical Fe dissolution. Moreover, the interaction between noble metal clusters and M–N–C can induce spin-state transitions, thereby enhancing ORR kinetics, as the spin configurations of active sites significantly influence orbital interactions.³²

The selection of metal particles for introduction requires careful consideration, especially under the demanding operating conditions of PEMFCs. In hybrid catalysts such as Pt–M alloys and M–N–C, the inevitable leaching of transition metals can lead to decreased catalytic activity and hinder proton conductivity and oxygen diffusion within ionomer layers, exacerbating performance degradation significantly.^{33–35}

In contrast to random alloys, ordered Pt–M intermetallic structures with strong Pt–M bonds can effectively mitigate metal dissolution.^{35–37} Therefore, the combination of M–N–C with intermetallic compounds can effectively improve the stability of the catalyst, which is expected to meet the long-term stability required for fuel cell operation.^{38–40} One major concern is to develop effective strategies to mitigate particle aggregation caused by the high-temperature annealing for phase transition and thus increase electrochemically active surface areas.^{41–44} Furthermore, the unclear synergistic effect underlying the M–N–C catalyst supported ordered Pt-base NPs must be elucidated to facilitate the rational design of durable catalysts.

In contrast to the potent Fenton effects associated with Fe-based species, Co–N–C emerges as a highly promising alternative to replace Fe–N–C.^{13,45} In this study, employing a range of advanced characterization techniques, we systematically examined a hybrid ORR catalyst comprising low-loading, ultrasmall intermetallic NPs and Co–N–C catalysts to address the aforementioned concerns. Specifically, L1₂-Pt₃Co alloys loaded onto Co–N–C hybrid catalysts, with an ultralow Pt loading of only 1.69 wt %, were synthesized by electronically coupling ordered Pt₃Co alloys with CoN₄ sites. Through X-ray photoelectron spectroscopy (XPS), X-ray absorption spectroscopy (XAS), and electrochemical results, we demonstrated that the strong electronic coupling interaction between ordered Pt₃Co alloys and the Co–N–C matrix significantly enhances the ORR activity and durability of Co–N–C. Compared to commercial Pt/C, the presence of multiple types of active sites increased the MA by 13.2 times. Notably, the catalyst exhibited

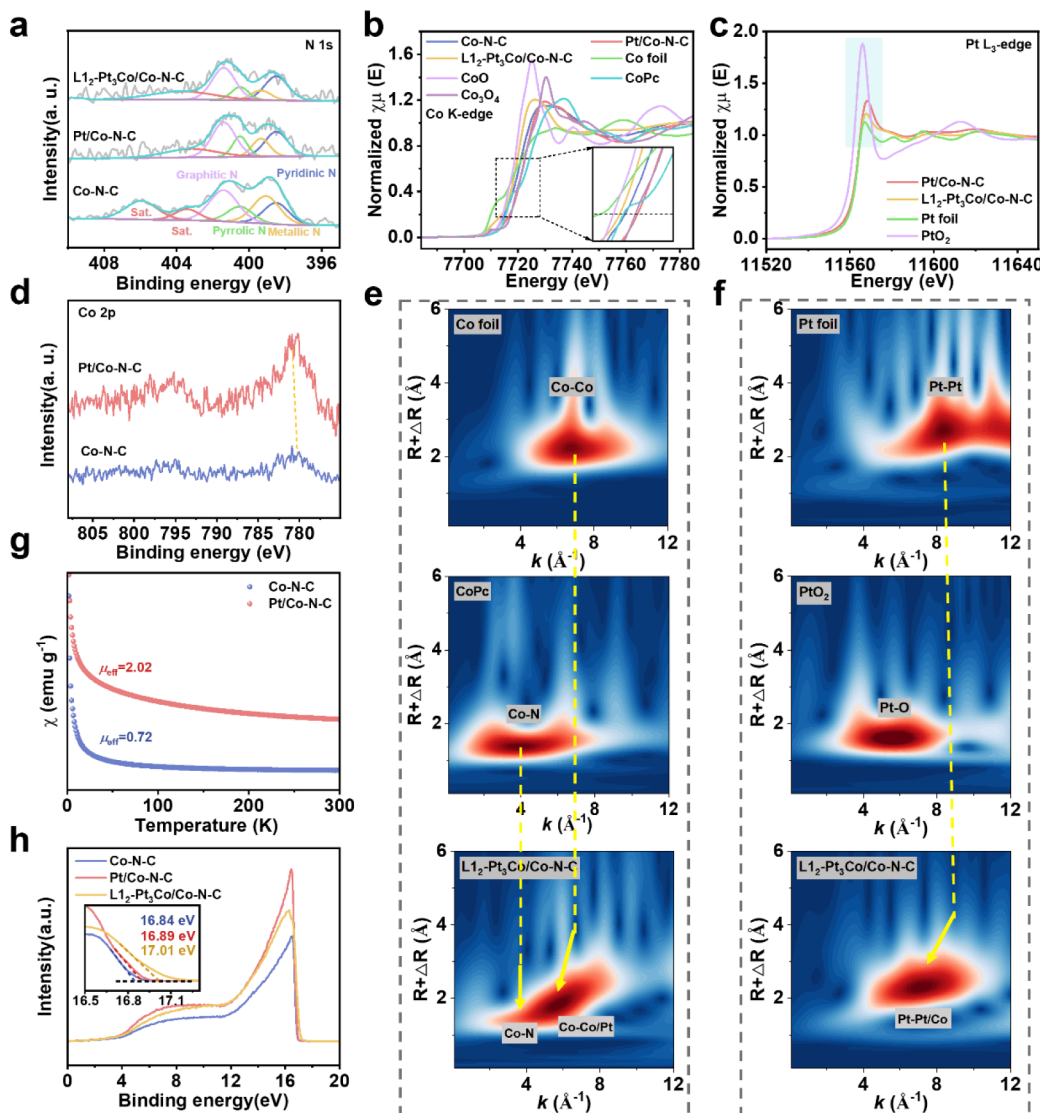


Figure 2. Electronic structure and coordination environment of catalysts. (a) N 1s XPS spectra of Co–N–C, Pt/Co–N–C, and L₁₂–Pt₃Co/Co–N–C. XANES spectra of the (b) Co K-edge and (c) Pt L₃-edge for L₁₂–Pt₃Co/Co–N–C and reference samples. (d) Co 2p XPS spectra of Co–N–C and Pt/Co–N–C. EXAFS WT analysis of the (e) Co K-edge and (f) Pt L₃-edge in the relevant samples. (g) Magnetic susceptibility of Co–N–C and Pt/Co–N–C. (h) Ultraviolet photoelectron spectroscopy of Co–N–C, Pt/Co–N–C, and L₁₂–Pt₃Co/Co–N–C. Inset: Local magnification.

stability with insignificant decay even after 80 000 cycles of potential cycling. The L₁₂–Pt₃Co/Co–N–C-based membrane electrode assembly (MEA) achieved an MA of 0.74 A mg_{Pt}⁻¹ at 0.9 V_{iR-free}, much higher than that of commercial Pt/C (0.25 A mg_{Pt}⁻¹ @ 0.9 V_{iR-free}). Moreover, the current density of the L₁₂–Pt₃Co/Co–N–C hybrid catalyst at 0.6 V remained nearly constant even after 120 h of operation. Density functional theory (DFT) calculations indicate that the strong electron coupling effect between Co–N–C and L₁₂–Pt₃Co NPs enhances the spin state of Co sites and strengthens the Co–N bond, thereby improving the activity and stability of Co–N–C.

RESULTS AND DISCUSSION

Morphology and Structure of Catalysts. The synthesis process of L₁₂–Pt₃Co/Co–N–C is schematically illustrated in Figure 1a, with experimental details provided in the Experimental Section. Briefly, Co–N–C was obtained by

pyrolyzing Co-doped ZIF-8. Subsequently, Pt NPs were reduced by ethylene glycol (EG) using Co–N–C as the carbon support, named Pt/Co–N–C. To alleviate the aggregation of Pt₃Co intermetallic NPs under high temperature, thin layers of zeolitic imidazolate framework (ZIF-67) were coated on Pt/Co–N–C, and then pyrolyzed at 800 °C under 5% H₂/Ar. The obtained product was denoted as L₁₂–Pt₃Co/Co–N–C.

As shown in Figure 1b, there is no characteristic diffraction peak of metallic Co in the X-ray diffraction (XRD) pattern of Co–N–C. The ordered L₁₂–Pt₃Co NPs in L₁₂–Pt₃Co/Co–N–C were confirmed by a well-matched standard PDF card (PDF#29-0499). The transmission electron microscopy (TEM) images display the good structural integrity of the rhombic dodecahedron of Co–N–C (Figure S1). The aberration-corrected high-angle annular dark-field scanning transmission electron microscopy (AC-HAADF-STEM) images confirmed the presence of atomic Co and a homogeneous elemental distribution (Figures S2 and S3). After H₂PtCl₆ was

reduced by alkaline EG, Pt NPs with an average size of ~2.05 nm were uniformly distributed on the Co–N–C matrix (Figures S4 and S5). The final L1₂-Pt₃Co/Co–N–C hybrid catalyst is obtained by acid etching the unstable metal component with 1 M HNO₃ after the resultant Pt/Co–N–C@ZIF-67 undergoes facile anneal treatment (Figure S6 and Table S1).^{46–48} The TEM images show uniformly distributed carbon-encapsulated L1₂-Pt₃Co NPs with a size of about 2.38 nm on the carbon support; the lattice spacing of 0.221 nm corresponds to the L1₂-Pt₃Co NPs (111) crystal plane (Figure S8). The L1₂-Pt₃Co NPs and atomic Co sites coexist in L1₂-Pt₃Co/Co–N–C (Figure 1c). Figure 1d illustrates a typical L1₂-Pt₃Co NP observed along the [110] axis.^{38,49} In line scan profiles based on different atomic brightness, alternating arrangements of different atoms within the particle interior can be observed by line profile-1 in Figure 1e; this is further corroborated by line profile-3 and line profile-4 in Figure S9.^{39,50} The Pt shell structure of L1₂-Pt₃Co NPs is evident after an acid leaching process, as evidenced by line profile-2 in Figure 1e. The results of the line scan in Figure 1g further confirm the existence of the Pt shell, and the relative intensity ratio of Pt to Co is close to 3, consistent with XRD results. As shown in Table S2, the inductively coupled plasma optical emission spectrometer (ICP-OES) detected that the Pt content in L1₂-Pt₃Co/Co–N–C is approximately 1.69 wt %, while the Co content is about 1.47 wt %. As a control, the average size of ordered Pt₃Co NPs synthesized by Co(NO₃)₂·6H₂O as the precursor is ~8.5 nm, much larger than our strategy, confirming that the ZIF-67 coating strategy can effectively inhibit particle agglomeration during the high-temperature process (Figures S10 and S11).^{40,50} In addition, this strategy is suitable for synthesizing ordered PtZn NPs (Figures S56–S58).

Raman spectroscopy and Brunauer–Emmett–Teller (BET) analysis were used to analyze the structural information on carbon in the catalyst. In the Raman spectrum (Figure S12), the D band and G band of carbon at 1350 and 1600 cm⁻¹ correspond to disordered sp³ carbon atoms and ordered sp²-hybridized carbon atoms in the ideal graphene layer, respectively.³⁴ Raman results show that the intensity ratio of D to G (I_G/I_D) for L1₂-Pt₃Co/Co–N–C is 1.02, similar to those for other Co–N–C and Pt/Co–N–C. BET results (Figure S13) showed that Co–N–C had the largest specific surface area (918.3 m² g⁻¹) and abundant micropores, which provided abundant anchor sites for Pt NPs. The specific surface areas of Pt/Co–N–C and L1₂-Pt₃Co/Co–N–C were reduced by the introduction of metal NPs.

The near-surface element composition, electron state, and local coordination structure of the catalysts were analyzed by XPS. As shown in Figure 2a, the main peaks in N 1s XPS spectra can be deconvoluted by pyridinic N (398.5 eV), metallic N (399.5 eV), pyrrolic N (400.5 eV), and graphitic N (401.4 eV).^{45,51} The explicit Co–N_x coordination exists in Co–N–C, Pt/Co–N–C, and L1₂-Pt₃Co/Co–N–C. The relative content of Co–N_x coordination in L1₂-Pt₃Co/Co–N–C is 0.28 at%, lower than that in Pt/Co–N–C (0.55 at%) (Table S3). The reduced content of metallic N indicates that Co species in the Co–N–C support served as one of the sources of Co to form L1₂-Pt₃Co NPs during secondary pyrolysis. As depicted in Figure 2d, Co elements mainly exist in the oxidation state of Co²⁺ in the Co–N_x species for Co–N–C and Pt/Co–N–C, and the Co 2p peak of Pt/Co–N–C exhibits a positive shift compared to Co–N–C, confirming the

electron transfer from Co sites to Pt NPs in Pt/Co–N–C. The Co 2p peak of L1₂-Pt₃Co/Co–N–C is shifted to the higher binding energy by about 1 eV compared to Pt/Co–N–C (Figure S14a). The Pt⁰ 4f peak of L1₂-Pt₃Co/Co–N–C has a negative shift of 0.3 eV compared with Pt/Co–N–C (Figure S14b).^{27,42} These results demonstrate strong electronic interaction between L1₂-Pt₃Co NPs and the Co–N–C support resulting from the charge transfer between the Co sites on Co–N–C and Pt in L1₂-Pt₃Co NPs in the hybrid catalyst.

XAS is utilized to probe the electronic structures and local coordination environments of all catalysts. X-ray absorption near edge structure (XANES) spectra of the Co K-edge and its linear fitting result show that the average valence of Co in Co–N–C is about 2.19, and the average valence of Co in Pt/Co–N–C is about 3.09 (Figures 2b and S15).⁵² This result indicates that the addition of Pt particles to Co–N–C causes electrons to shift from Co to Pt, resulting in an increase in the valence state of Co. Combined with XPS results, it confirms the strong electronic interaction between Pt particles and Co–N–C in the Pt/Co–N–C catalyst (Figure 2d). As shown in Figure 2c, the white line intensity of the Pt L₃-edge decreases in the following order: PtO₂ > Pt/Co–N–C > L1₂-Pt₃Co/Co–N–C > Pt foil, and its fitting result shows that the average valence of Pt in Pt/Co–N–C is about 1.07, and the average valence of Pt in L1₂-Pt₃Co/Co–N–C is about 0.43 (Figure R16), consistent with XPS results. The Co and Pt coordination environments in Pt/Co–N–C and L1₂-Pt₃Co/Co–N–C are verified by Fourier transform extended X-ray absorption fine structure (FT-EXAFS) spectra and wavelet transform (WT) analysis (Figures S17–S19 and 2e,f). The prominent main peak at 1.52 Å in Pt/Co–N–C can be attributed to Co–N/O coordination with a coordination number (CN) of 4.0, inheriting the coordination configuration of Co in Co–N–C (Figure S17 and Table S4). In the case of L1₂-Pt₃Co/Co–N–C, Co is present at both 1.71 Å as Co–N/O coordination (CN = 3.7) within Co–N–C and around 2.37 Å as Co–Co/Pt coordination within L1₂-Pt₃Co NPs (Figure S18 and Table S4). As shown in Figure S19, the FT-EXAFS spectrum of the Pt L₃-edge of L1₂-Pt₃Co/Co–N–C indicates a peak at about 2.33 Å attributed to the merged scattering paths of Pt–Pt and Pt–Co bonds, notably lower than the Pt–Pt coordination in Pt foil and Pt/Co–N–C ($R \approx 2.66$ Å). The fitting results of the shortened Pt–Pt bond length further confirmed the compression strain in L1₂-Pt₃Co NPs induced by the introduction of Co, which is more conducive to reducing the d-band center of Pt atoms and weakening the strong adsorption of Pt to oxygen-containing species (Figure S19 and Table S4).^{53,54}

The transfer of electrons from oxygen species to metal sites during ORR evolves spin-electrons from paramagnetic oxygen species to diamagnetic intermediates.⁵⁵ The active site spin configurations strongly affect orbital interactions, which affect the ORR process.^{55–57} To characterize the change in the magnetic properties of catalysts, the effective magnetic moments (μ_{eff}) of the catalysts were determined by vibrating sample magnetometer (VSM) (Figures 2g and S20).^{56,58} The μ_{eff} of Co–N–C is 0.72, while the μ_{eff} of Pt/Co–N–C is 2.02. The number of unpaired electrons (n) at the Co sites within Co–N–C is determined to be about 0, whereas the n at the Co sites within Pt/Co–N–C is about 1 (Figure 2g). According to previous research, the strong electronic interaction between Pd nanoclusters and the Fe single atom successfully induces the spin-state transition of Fe sites from

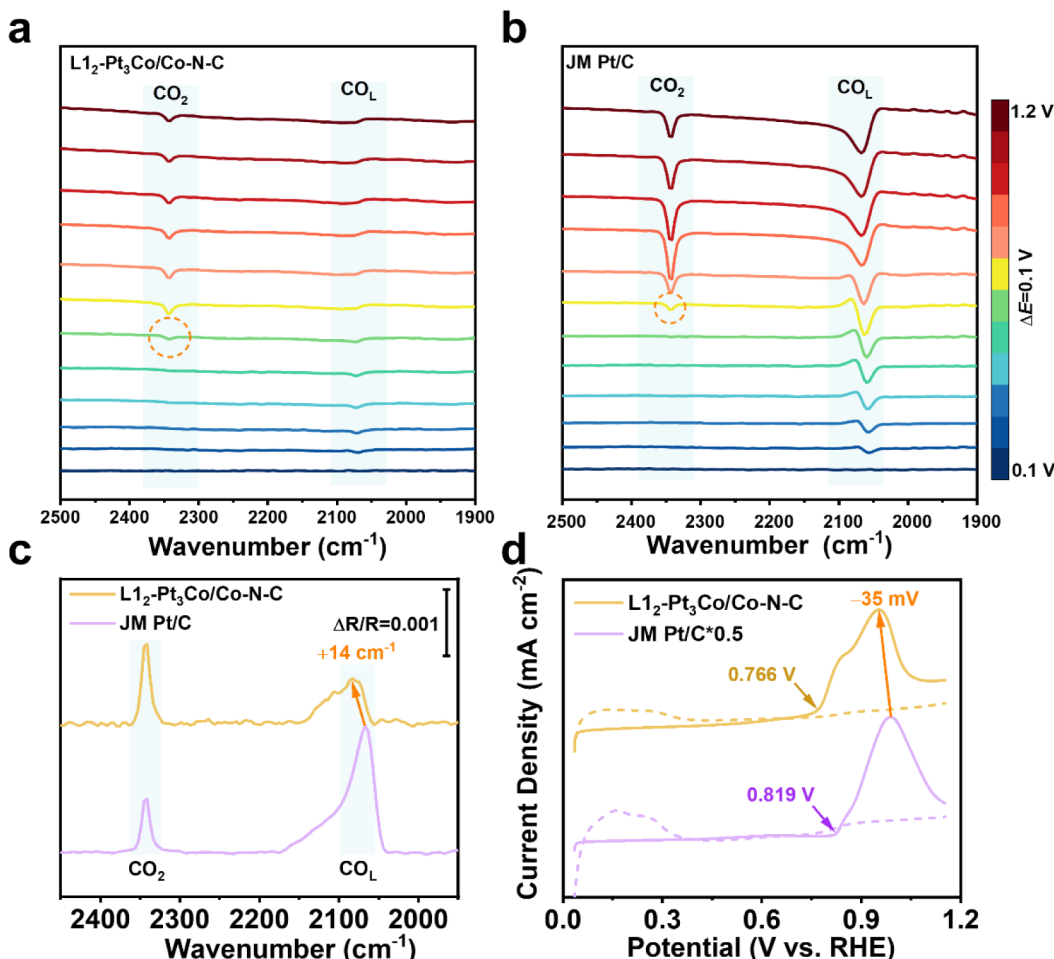


Figure 3. Surface chemical nature of L₁₂-Pt₃Co/Co-N-C. Multipotential *in situ* FTIR spectra of CO adsorbed on the (a) L₁₂-Pt₃Co/Co-N-C and (b) JM Pt/C in 0.1 M HClO₄. The reference potential was 0.1 V (vs RHE). (c) CO adsorbed FTIR spectra of L₁₂-Pt₃Co/Co-N-C and JM Pt/C. The reference potential was 1.2 V. (d) CO-stripping curves of L₁₂-Pt₃Co/Co-N-C and JM Pt/C in N₂-saturated 0.1 M HClO₄ with a scanning rate of 50 mV s⁻¹.

low spin to intermediate spin, making the ORR preferably proceed *via* a dissociative pathway and accelerating the removal of oxygen species.³² Therefore, the introduction of Pt NPs in Co–N–C can alleviate the strong electron transfer between the surface/interface of Co sites and the oxygen-containing intermediate, reducing the adsorption strength of Co sites and oxygen species, thus accelerating the ORR process. Due to the interference of metallic Co, it is difficult to distinguish the spin-state of Co sites within L₁₂-Pt₃Co/Co-N-C (Figure S20). However, it can be confirmed that the alloying strategy is beneficial to further reduce the charge transfer energy barrier during ORR.^{32,59} Figure 2h displays distinct differences in the secondary cutoff energies (E_{cutoff}) for the catalysts, where the E_{cutoff} of Co–N–C, Pt/Co–N–C, and L₁₂-Pt₃Co/Co-N-C is 16.84, 16.89, and 17.01 eV, respectively. The L₁₂-Pt₃Co/Co-N-C exhibits the lowest work function ($\Phi = 4.21$ eV), suggesting that the hybrid catalyst has the smallest electron transfer energy barrier with oxygen-containing intermediates.

We performed *in situ* electrochemical FTIR spectroscopy of surface-adsorbed CO to reveal the surface chemical nature of L₁₂-Pt₃Co/Co-N-C.^{60–63} Figure 3a,b shows the *in situ* FTIR spectra of CO adsorbed on JM Pt/C and L₁₂-Pt₃Co/Co-N-C. The band at 2050 cm⁻¹ is assigned to linear-adsorbed CO (CO_L) on Pt, while the band located near 2350 cm⁻¹ is

attributed to CO₂ produced from CO oxidation. The direction of the adsorbed CO band is reversed due to the abnormal infrared effects of the adsorbed species on nanomaterials. The signal of CO₂ can be observed during the potential increase. Clearly, the CO₂ signal on L₁₂-Pt₃Co/Co-N-C can be observed at 0.6 V, while the CO₂ signal on JM Pt/C can be observed at 0.7 V. Typically, weaker CO surface chemisorption energy would increase the C–O binding energy in the CO molecule and thus increase their C–O stretching frequency. The IR band of CO_L is blue-shifted from 2065 cm⁻¹ on Pt/C to 2076 cm⁻¹ on L₁₂-Pt₃Co/Co-N-C (Figure 3c). L₁₂-Pt₃Co/Co-N-C exhibits a weaker CO chemisorption energy than Pt/C, indicating a decreased corresponding surface reactivity. Similar results can be observed from CO-stripping curves. As shown in Figure 3d, the onset potential of CO oxidation for L₁₂-Pt₃Co/Co-N-C and JM Pt/C occurs at 0.766 and 0.819 V, respectively.^{40,61} The CO oxidation peaks for L₁₂-Pt₃Co/Co-N-C undergo a negative shift (35 mV) compared to JM Pt/C, which may be due to the introduction of Co sites in the carbon support and the alloying of Pt NPs reducing the *d*-band center of Pt, resulting in weakened adsorption strength of OH upon the Pt surface, which is more conducive to ORR kinetics.^{53,54} It is generally accepted that the electrochemical oxidation of CO proceeds according to the Langmuir–Hinshelwood mechanism, including water dissoci-

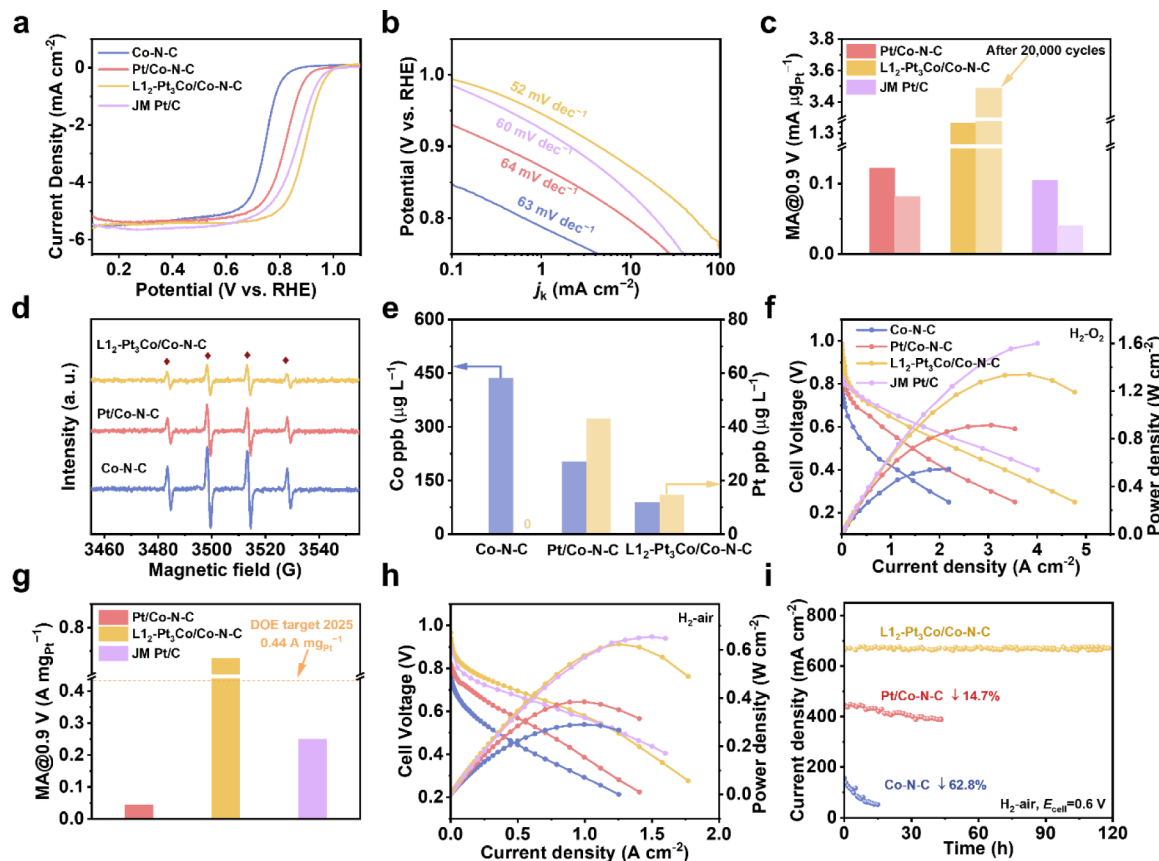


Figure 4. ORR performance of catalysts. (a) LSV curves and (b) Tafel plots for Co–N–C, Pt/Co–N–C, L1₂–Pt₃Co/Co–N–C, and JM Pt/C. (c) MA values (@0.9 V) for the studied catalysts before and after 20 000 ADT cycles at RT. (d) EPR spectra of Co–N–C, Pt/Co–N–C, and L1₂–Pt₃Co/Co–N–C with DMPO as a molecular probe of *OH and 0.1 M HClO₄ as solvent. (e) The amount of Co ions and Pt ions dissolved in the electrolyte obtained from ICP-MS for Co–N–C, Pt/Co–N–C, and L1₂–Pt₃Co/Co–N–C catalyst after 10 000 ADT cycles at RT. (f) H₂–O₂ fuel cell polarization curves and power density plots for Co–N–C, Pt/Co–N–C, L1₂–Pt₃Co/Co–N–C, and JM Pt/C as cathodes in MEA. Anode: 0.1 mg_{Pt} cm⁻² for JM Pt/C; cathode: 2 mg_{catalyst} cm⁻² for Co–N–C, Pt/Co–N–C, and L1₂–Pt₃Co/Co–N–C; 0.1 mg_{Pt} cm⁻² for JM Pt/C. Membrane: Nafion 211; temperature: 80 °C; backpressure: 150 kPa (absolute). (g) MA values (@0.9 V) for the studied catalysts derived from the H₂–O₂ fuel cell measurement. The dotted orange line denotes the US DOE target for 2025. (h) H₂–air fuel cell polarization and power density plots for Co–N–C, Pt/Co–N–C, L1₂–Pt₃Co/Co–N–C, and JM Pt/C as cathodes in the MEA. (i) Chronoamperometric curves of Co–N–C, Pt/Co–N–C, and L1₂–Pt₃Co/Co–N–C at 0.6 V vs RHE.

ation to produce OH groups, and the following CO_{ad} oxidation via the interaction with adsorbed OH.^{64,65} As discussed above, the *d*-band of L1₂–Pt₃Co/Co–N–C was downshifted, leading to a weaker *d*–π* interaction with the adsorbed CO.

ORR Performance. The electrochemical area of the catalysts was first evaluated by cyclic voltammetry curves and CO-stripping curves in 0.1 M HClO₄ electrolyte (Figure S22). According to the charge of CO oxidation in the CO-stripping curves, the electrochemically active surface areas (ECSAs) of the catalysts are calculated to be 97.6, 82.1, 77.8, and 86.9 m² g_{Pt}⁻¹ for Pt/Co–N–C, L1₂–Pt₃Co/C, L1₂–Pt₃Co/Co–N–C, and JM Pt/C, respectively (Figure S22). As shown in Figure 4a, the half-wave potential (*E*_{1/2}) of the Co–N–C is 0.746 V (vs RHE). With the addition of Pt, the *E*_{1/2} of Pt/Co–N–C positively shifted 73 mV. After carbon coating and alloying treatment, the L1₂–Pt₃Co/Co–N–C hybrid catalyst showed ORR activity with an *E*_{1/2} of 0.895 V. The MA and specific activity (SA) of L1₂–Pt₃Co/Co–N–C were 1.385 mA µg_{Pt}⁻¹ and 1.779 mA cm⁻², 13.2 times and 14.7 times greater than that of JM Pt/C, respectively (Table S5). L1₂–Pt₃Co/Co–N–C exhibited the lowest Tafel slope (52 mV dec⁻¹), corresponding to the fastest ORR dynamics (Figure 4b). By comparing the ORR activity of L1₂–Pt₃Co/Co–N–C and L1₂–

Pt₃Co/C, the synergistic effect between Co–N–C and L1₂–Pt₃Co NPs in the L1₂–Pt₃Co/Co–N–C hybrid catalyst was confirmed (Figure S23). Figure S24 shows the selectivity for the ORR tested by the rotating ring disk electrode (RRDE). The H₂O₂ yield was 21.4% for Co–N–C at 0.75 V, and the addition of Pt NPs can significantly suppress H₂O₂% to 3.8%. Furthermore, L1₂–Pt₃Co/Co–N–C exhibited the lowest H₂O₂ yield (0.9%), indicating that L1₂–Pt₃Co NPs are conducive to the rapid reduction of H₂O₂.

The stability of all catalysts was demonstrated by an accelerated durability test (ADT) with a potential range of 0.6–1.0 V in a N₂-saturated 0.1 M HClO₄ electrolyte at room temperature (RT) (Figures S25–S31 and Table S5). In Figures S25 and S26, after 20 000 ADT cycles at RT, the *E*_{1/2} of Co–N–C shifted negatively by 50 mV, while it only shifted negatively by 20 mV for Pt/Co–N–C. More interestingly, L1₂–Pt₃Co/Co–N–C demonstrated better durability than JM Pt/C. After 20 000 ADT cycles at RT, the MA of L1₂–Pt₃Co/Co–N–C increased from 1.385 to 3.487 mA µg_{Pt}⁻¹, 87.2 times higher than that of JM Pt/C after ADT (Figure 4c and Table S5). After 80 000 ADT cycles of L1₂–Pt₃Co/Co–N–C at RT, its MA retained 1.599 mA µg_{Pt}⁻¹, far exceeding the United States Department of Energy 2025 targets (0.44 A mg_{Pt}⁻¹ for

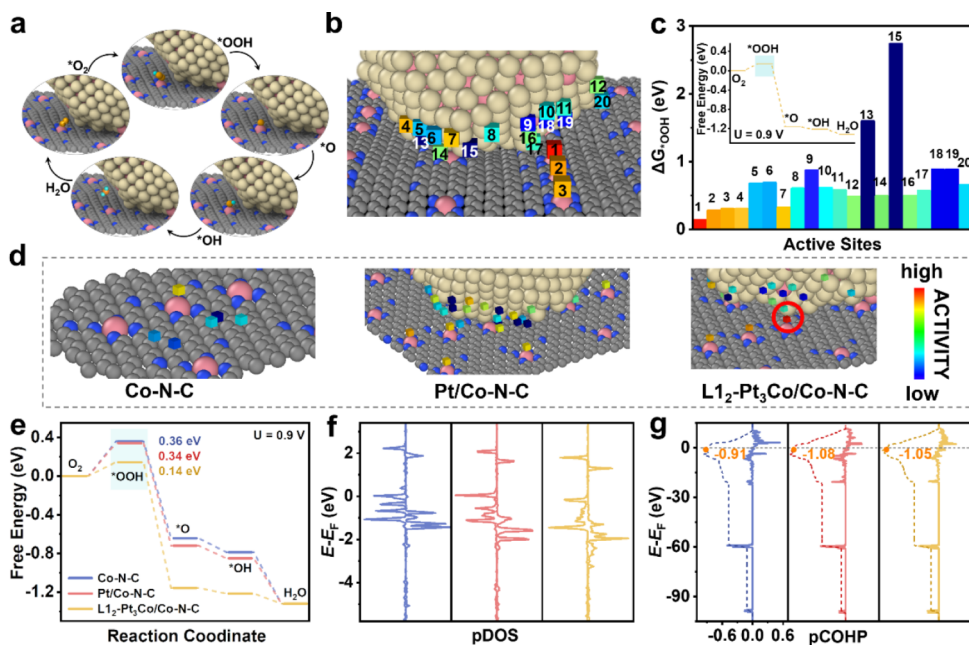


Figure 5. Study on the mechanism of catalysts. (a) Schematic ORR pathway on the Co–N₄ site adjacent to L₁₂–Pt₃Co NPs in L₁₂–Pt₃Co/Co–N–C. (b) Multiple active sites and (c) their corresponding O₂ → *OOH reaction energy barriers in L₁₂–Pt₃Co/Co–N–C. Inset: Example of a free energy diagram for multiple sites in L₁₂–Pt₃Co/Co–N–C. (d) Diagram of ORR activity at multiple sites in the models of Co–N–C, Pt/Co–N–C, and L₁₂–Pt₃Co/Co–N–C. The redder the color box, the higher the ORR activity of the corresponding active site, while the bluer the color block, the opposite result. (e) Free energy diagram of the Co–N₄ site within Co–N–C, Pt/Co–N–C, and L₁₂–Pt₃Co/Co–N–C for ORR at 0.9 V. * represents the active site. (f) The pDOS of Co within Co–N₄ for Co–N–C, Pt/Co–N–C, and L₁₂–Pt₃Co/Co–N–C. (g) pCOHP of Co–N₄ for Co–N–C, Pt/Co–N–C, and L₁₂–Pt₃Co/Co–N–C.

MA) (Figure S28).⁶⁶ Furthermore, to simulate the operating conditions of fuel cell testing, ADT was also conducted at 60 °C (Figures S32–S37 and Table S6). After 10 000 ADT cycles, the MA of L₁₂–Pt₃Co/Co–N–C remained at the initial 38.8%, whereas the MA of JM Pt/C was only retained at the initial 12.1% (Figure S37 and Table S6).

Generally, the deterioration of M–N–C catalysts can be significantly governed by the demetalation induced by H₂O₂ attack. To assess the activity of the Fenton reaction and the susceptibility of the catalyst attacked by •OH during ORR, 2,2'-azinobis(3-ethylbenzothiazoline-6-sulfonate) (ABTS) was used as a molecular probe to test the UV/vis spectrum to compare the intensity of the Fenton reaction, and 5,5-dimethyl-1-pyrroline N-oxide (DMPO) was employed to test EPR spectra to simulate the difference in the affinity of different samples to •OH.^{11,67} As shown in Figure S38, the absorbance at 417 nm for Co–N–C + ABTS + H₂O₂, Pt/Co–N–C + ABTS + H₂O₂, and L₁₂–Pt₃Co/Co–N–C + ABTS + H₂O₂ decreases sequentially, with values of 1.52, 1.21, and 0.91, respectively. As shown in Figure 4d, the 1:2:2:1 peak corresponds to the –DMPO–OH adduct, and the peak intensity for Co–N–C, Pt/Co–N–C, and L₁₂–Pt₃Co/Co–N–C is 0.71, 0.44, and 0.26, respectively. These results indicate that the Co site in Co–N–C has a strong Fenton effect and strong binding with •OH. The introduction of L₁₂–Pt₃Co NPs results in lower Fenton reaction activity and strong •OH resistance of the Co–N–C compared to Pt/Co–N–C, facilitating ORR activity and stability. Figures S40 and 4e demonstrate that the introduction of Pt NPs can greatly alleviate the leaching of active Co sites during ADT. The Co–N–C catalyst dissolved 437 ppb into the electrolyte during the ORR, while Pt/Co–N–C dissolved only 203 ppb. The above results confirm the stabilizing effect of Pt particles on the active

Co sites within Co–N–C. As shown in Figure S41, the active Co sites of the Co–N–C catalyst were severely leached after ADT. The relative content of Co²⁺ in Co–N–C after ADT decreased by 22.22 at%, and the relative content of metallic N decreased by 44.58 at%, in comparison to pristine Co–N–C. For the Pt/Co–N–C catalyst, there was no significant change in the electronic structure of the active Co site after ADT, and the relative content of metallic N only decreased by 16.67 at% (Figure S42). Figures S43 and S44 indicate that Pt/Co–N–C exhibits significant particle aggregation and growth after 10 000 ADT cycles, with an average particle size of about 3 nm, while L₁₂–Pt₃Co NPs in L₁₂–Pt₃Co/Co–N–C remain uniformly dispersed. Therefore, compared to other advanced catalysts, the L₁₂–Pt₃Co/Co–N–C hybrid catalyst exhibits outstanding ORR stability in a rotating disk electrode (RDE) (Table S7).

The H₂–O₂ single cell assembled by the cathode L₁₂–Pt₃Co/Co–N–C catalyst achieved a current density of 1.38 A cm⁻² at a voltage of 0.6 V and a peak power density (P_{max}) of 1.34 W cm⁻² with a loading of 0.034 mg_{pt} cm⁻² (Figure 4f). The performance of L₁₂–Pt₃Co/Co–N–C far exceeds that of Co–N–C and Pt/Co–N–C with the same catalyst loading (loading: 2 mg_{catalyst} cm⁻²) with P_{max} values of 0.55 and 0.91 W cm⁻², respectively, slightly lower than that of commercial Pt/C catalysts with a P_{max} value of 1.60 W cm⁻² (loading: 0.1 mg_{pt} cm⁻²). The MA at 0.9 V_{R-free} of L₁₂–Pt₃Co/Co–N–C (0.74 A mg_{pt}⁻¹) exceeds the target of the US DOE for 2025, 3.0 times higher than Pt/C (Figures 4g and S45). Likewise, in Figure 4h, the performance of the H₂–air single cell with L₁₂–Pt₃Co/Co–N–C as a cathode catalyst delivers a P_{max} of 0.60 W cm⁻², comparable to that of commercial Pt/C (0.64 W cm⁻²). These results show that the alloying of Pt NPs and the synergistic interface effect between Co–N–C and L₁₂–Pt₃Co NPs greatly improve the electrocatalytic performance. In addition, after

operating at 0.6 V for 15 h, the current density of Co–N–C and Pt/Co–N–C is reduced by 62.8 and 5.4%, respectively (**Figure 4i**), and the current density of Pt/Co–N–C is reduced by 14.7% after operating at 0.6 V for 45 h, confirming the promotion effects of Pt NPs on durability. More strikingly, the current density of L₁₂-Pt₃Co/Co–N–C barely changed even after 120 h of operation, indicating that the protection effect of L₁₂-Pt₃Co NPs on the Co–N–C catalyst was much better than that of Pt NPs on the Co–N–C catalyst.

DFT Calculations. First-principles-based analysis is employed to achieve an atomic-scale understanding of the ORR on Pt₃Co NPs and CoN₄. Considering the complexity of the interface structure, we utilized machine learning potentials (MLPs) to construct models of the interface. Through the utilization of machine learning-based potential annealing simulations, we successfully acquired structures that align with experimental observations in terms of size and atomic arrangement in the ordered Pt₃Co alloy nanoparticles. Our models consist of an intricate interfacial system that encompasses Co–N₄ single-atom sites, carbon support, and metal nanoparticles. The simulation process is detailed in the **Supporting Information mp4 files**, while the simulated results are presented in **Figures S46 and S47**. Simulation details, including force field construction, machine learning parameters, and simulation details, are available in **Section 2 of the Supporting Information**.

We employ the computational hydrogen electrode method to specifically investigate the activity of the sites. To more comprehensively consider the diversity of sites in the interface model, we calculate the Gibbs free energy of ORR on around 20 interface sites in each model to reveal the most active sites in the catalysts (**Figures 5b** and **S48–S53**). The rate-limiting step of the ORR is the formation of *OOH. In **Figure S50**, site-1 in Co–N–C exhibits the lowest energy barrier (with the largest Gibbs energy difference of 0.36 eV), confirming that the metal centers are the active sites of M–N–C. In **Figure 5c**, site-1 in L₁₂-Pt₃Co/Co–N–C exhibits the highest ORR activity with an energy barrier of 0.14 eV. To make it easier to understand, we visualize the energy barrier in **Figure 5d**, and the redder the box, the higher the activity. From the results, we discern that the best active site (red circle) is located at the Co–N₄ site adjacent to L₁₂-Pt₃Co NPs, superior to the well-known activity of Pt sites. These results demonstrate that adjacent noble metal NPs boost the ORR activity of Co–N–C via strong interactions. Compared with single atoms farther away from L₁₂-Pt₃Co, those closer to L₁₂-Pt₃Co NPs exhibit notably enhanced activity. Hence, a reasonable inference is that the introduction of L₁₂-Pt₃Co and Pt NPs enhances the activity of the Co–N–C catalyst, with L₁₂-Pt₃Co NPs exerting a greater effect compared to Pt NPs (**Figure 5e**). More precisely, the introduction of L₁₂-Pt₃Co NPs and Pt NPs leads to a decreased adsorption of oxygen species by Co–N₄, thereby boosting the reactivity of the ORR. We conducted an electronic structure analysis to explore the origin of activity enhancement. From the projected electronic density of states (pDOS) of Co within Co–N₄ (**Figure 5f**), it is apparent that the pDOS of the atomic Co sites are highly asymmetric, signifying high spin density.¹² To quantify this, we calculated the spin density values of Co within Co–N₄ in these three models, finding a ranking of Co [Co–N₄] < Co [Co–N₄–Pt NPs] < Co [Co–N₄–L₁₂-Pt₃Co NPs] (0.63 vs 0.92 vs 1.01, **Figure S54**), consistent with the results of VSM. This indicates that L₁₂-Pt₃Co NPs and Pt NPs can enhance the spin density

of Co, serving as the source of reactivity. Furthermore, we analyzed the work functions of L₁₂-Pt₃Co NPs and Pt NPs, which are 5.4 and 5.7 eV, respectively. This implies that the lower Fermi energy level (E_F) of L₁₂-Pt₃Co NPs can allow more electrons transferred from Co to be accommodated, thereby enhancing the spin density of Co within Co–N₄. **Figures 5g** and **S55** show that the COHP of the Co–N bond near Pt NPs and L₁₂-Pt₃Co NPs increases from −0.91 to −1.08 and −1.05, respectively, indicating that the Co–N bond becomes stronger under the action of the surrounding Pt NPs and L₁₂-Pt₃Co NPs, confirming the previous hypothesis. In short, the introduction of precious metal particles can enhance the stability of the Co–N bond in Co–N–C and alleviate the leaching of Co sites, consistent with the previous ICP results (**Figure 4d**).

CONCLUSION

We report the successful synthesis of a hybrid ORR electrocatalyst comprising atomically dispersed Co sites and L₁₂-Pt₃Co NPs. This hybrid catalyst demonstrates outstanding ORR activity and durability in RDE measurements alongside high power density and stability in H₂–air/O₂ fuel cells. In an acidic electrolyte, the half-wave potential of L₁₂-Pt₃Co/Co–N–C is 0.895 V, significantly surpassing that of Pt/Co–N–C and Co–N–C. Following 20 000 cycles in the potential range of 0.6–1.0 V, the $E_{1/2}$ increases to 0.939 V, with a corresponding MA of 3.487 mA $\mu\text{g}_{\text{Pt}}^{-1}$. Assembled in a H₂–O₂ single cell, the P_{max} reaches 1.34 W cm^{−2}, with a loading capacity of 0.034 mg_{pt} cm^{−2}, and a back pressure of 150 kPa. Notably, the current density at 0.6 V remains stable over 120 h. The synergistic effect between Co–N–C and L₁₂-Pt₃Co NPs in L₁₂-Pt₃Co/Co–N–C effectively inhibited the leaching of Co sites in Co–N–C and the dissolution of Pt atoms in L₁₂-Pt₃Co NPs. DFT calculations further confirm the interaction between Co sites and NPs, along with stabilization of Co sites in Co–N–C by L₁₂-Pt₃Co NPs. Our results highlight the importance of the synergistic effects among different active sites in hybrid electrocatalysts, offering an alternative approach to designing more active and durable M–N–C electrocatalysts for fuel cells and other electrochemical devices.

EXPERIMENTAL SECTION

Chemicals. Zinc nitrate hexahydrate (Zn(NO₃)₂·6H₂O, AR, Aldrich), cobalt nitrate hexahydrate (Co(NO₃)₂·6H₂O, AR, Sinopharm), 2-methylimidazole (AR, Aldrich), chloroplatinic acid (H₂PtCl₆, Kunming Institute of Precious Metals), potassium hydroxide (KOH, AR, Sinopharm), 1,10-phenanthroline (AR, Aldrich), methanol (AR, Sinopharm), ethanol (AR, Sinopharm), ethylene glycol (EG, AR, Sinopharm), hydrochloric acid (HCl, GR, 36%, Sinopharm), perchloric acid (HClO₄, GR, 70%, Sinopharm), Nafion solution (D520, 5 wt %, Alfa-Aesar), and isopropyl alcohol(IPA, AR, Macklin) were used as received. All solutions were prepared with ultrapure water (18.2 MΩ cm). 20 wt % Pt/C catalyst from Johnson Matthey (JM Pt/C) was used as received.

Synthesis of Co–N–C Catalyst. The Co–N–C catalyst was synthesized via a soft-template pyrolysis method. Typically, 4 g of 2-methylimidazole was dissolved into 100 mL methanol solution to form a homogeneous transparent solution, referred to as solution A. Additionally, 2 g of Zn(NO₃)₂·6H₂O and 600 mg of Co(NO₃)₂·6H₂O were dissolved into 100 mL of methanol solution to form a uniform solution, referred to as solution B. After mixing solutions A and B, the reaction temperature was increased to 60 °C and held for 24 h to allow Co-doped ZIF-8 nanocrystals to grow. After being cooled to room temperature, the Co-ZIF-8 nanocrystals were collected by centrifugation, washed at least three times with methanol, and dried at

60 °C in a vacuum oven for 5 h. The Co-ZIF-8 precursors were subsequently heated at a temperature of 1100 °C in a tube furnace under Ar for 1 h (10 °C min⁻¹) to obtain the Co- and N-codoped nanocarbon (Co–N–C) catalyst.

Synthesis of Pt/Co–N–C Catalyst. Co–N–C served as the carbon support, and Pt nanoparticles were reduced *in situ* on Co–N–C by the alkaline EG reduction method. 45 mg of KOH was added to 20 mL of EG solution containing 1 mg of H₂Cl₆Pt, which was ultrasonicated and stirred to form a uniform light-yellow solution. The solution was heated to 160 °C for 5 min in a microreactor at 80 W to form a homogeneous suspension and then washed with a 1 M aqueous solution of HCl in a volume ratio of around 1:1. The dark precipitate was centrifuged at 7000 rpm for 5 min. This washing step was repeated twice to remove any remaining EG or KOH. The above precipitates were added to 40 mL ethanol solution containing 38 mg of Co–N–C and treated with ultrasound for 2 h. The black precipitate was filtered and dried at 60 °C in a vacuum oven for 5 h. The obtained powders were denoted as Pt/Co–N–C catalyst.

Synthesis of L1₂-Pt₃Co/Co–N–C Catalyst. The Pt to Co ratio, heat treatment temperature, and holding time were adjusted to determine the synthesis parameters for small L1₂-Pt₃Co intermetallic compounds during this synthesis process (Figure S7). The optimized experimental steps are as follows: 123 mg of 2-methylimidazole was dissolved into 10 mL of methanol solution to form a homogeneous transparent solution, referred to as solution A. 20 mg of Pt/Co–N–C and 108 mg of Co(NO₃)₂·6H₂O were dissolved into 10 mL of methanol to form a uniform solution, referred to as solution B. Solutions A and B were mixed and stirred for 2 h at room temperature (RT), then collected by centrifugation, washed at least three times with methanol, and dried at 60 °C in a vacuum oven for 5 h. The ZIF-67-coated Pt/Co–N–C was subsequently heated at a temperature of 800 °C for 1 h in flowing 5% H₂/Ar with a heating rate of 5 °C min⁻¹ in a tube furnace to obtain the L1₂-Pt₃Co/Co–N–C. The 20 mg of L1₂-Pt₃Co/Co–N–C was soaked in 10 mL of 1 M HNO₃ aqueous solution, sonicated for 2 h at room temperature, and subsequently separated using a filtration device and rinsed with water.

Synthesis of L1₂-Pt₃Co/C Catalyst. The PtCo/C was fabricated following similar procedures as for L1₂-Pt₃Co/Co–N–C. The carbon support is Ketjen Black ECP600JD instead of Co–N–C.

Traditional Synthesis of L1₂-Pt₃Co/Co–N–C Catalyst. 20 mg of the synthesized Pt/Co–N–C powder was moistened, 20 mg of 1,10-phenanthroline, 5 mg of Co(NO₃)₂·6H₂O, and 20 mL of ethanol were added and dispersed evenly. The above solution was placed on a heating stage at 80 °C and stirred until the solvent evaporated completely. The black powder was subsequently heated at a temperature of 750 °C for 3 h in flowing 5% Ar/H₂ with a heating rate of 10 °C min⁻¹ in a tube furnace. The obtained powders were denoted as L1₂-Pt₃Co/Co–N–C–Co(NO₃)₂.

Catalysts Characterization. Transmission electron microscopy (TEM), high-resolution (HR)TEM, and elemental mapping were acquired on a JEOL JEM-F200 with an electron acceleration voltage of 200 kV. Aberration-corrected high-angle annular dark-field scanning transmission electron microscopy (AC-HAADF-STEM) images and energy-dispersive X-ray spectroscopy (EDS) mapping images were recorded on a Titan 80-300 scanning/transmission electron microscope operated at 300 kV, equipped with a probe spherical aberration corrector. X-ray diffraction (XRD) measurements were characterized by an X'Pert PRO X-ray Diffractometer using copper K α radiation ($\lambda = 1.5406 \text{ \AA}$) at 40 kV, 40 mA. Surface areas and pore structures of the catalysts were measured by nitrogen physisorption analysis using an Autosorb-IQ2-MP instrument operated at -196 °C. Before measurement, degassing of the powder samples was done at 140 °C overnight under a continuous flow of N₂ gas to obtain a clean surface. A multipoint Brunauer–Emmett–Teller (BET) model was employed to estimate the surface areas. The corresponding pore size distribution parameters were obtained from the adsorption isotherm by the DFT method. Raman measurements were performed on a Thermo DXR 2xi. X-ray photoelectron spectroscopy (XPS) measurements were performed with an ESCA LAB 250 spectrometer by using Al K α irradiation. The X-ray

absorption spectra (XAS) including X-ray absorption near-edge structure (XANES) spectra and extended X-ray absorption fine structure (EXAFS) spectra of the sample at the Co K-edge and Pt L₃-edge were collected at the Beamline of TPS44A1 in the National Synchrotron Radiation Research Center (NSRRC), Taiwan. 3.0 GeV a pair of channel-cut Si (111) crystals was used in the monochromator. Ultraviolet photoelectron spectroscopy (UPS) measurements were performed on a Thermo Nexsa. Electron paramagnetic resonance (EPR) measurements were performed on a Bruker EMX plus. Vibrating sample magnetometer (VSM) measurements were performed by a 7404 instrument from Lake Shore Cryotronics. Ultraviolet-visible spectrophotometer (UV-vis) measurements were performed on a Thermo EVOLUTION220. Inductively coupled plasma-optical emission spectrometry (ICP-OES) measurements were carried out on Agilent 5110. Inductively coupled plasma-mass spectrometry (ICP-MS, Autosorb-IQ2-MP) was used to determine the total Co and Pt contents in 0.1 M HClO₄ electrolyte after the accelerated durability test (ADT).

ASSOCIATED CONTENT

SI Supporting Information

The Supporting Information is available free of charge at <https://pubs.acs.org/doi/10.1021/acsnano.4c06615>.

Data analysis, electrochemical tests, details of DFT calculation, and additional physical/electrochemical characterization data: TEM images, STEM images, mapping results, XRD patterns, Raman spectra, BET results, XPS spectra, XAS spectra, ICP-OES, and ORR performance curves (PDF)

Optimization model video of L1₂-Pt₃Co/C for DFT calculation (MP4)

Optimization model video of L1₂-Pt₃Co/Co–N–C for DFT calculation (MP4)

Optimization model video of Pt/Co–N–C for DFT calculation (MP4)

Optimization model video of Co–N–C for DFT calculation (MP4)

AUTHOR INFORMATION

Corresponding Authors

Bang-An Lu – College of Materials Science and Engineering, Zhengzhou University, Zhengzhou 450001, P.R. China;
✉ orcid.org/0000-0002-4532-598X; Email: zjn@zzu.edu.cn

Jia-Nan Zhang – College of Materials Science and Engineering, Zhengzhou University, Zhengzhou 450001, P.R. China;
✉ orcid.org/0000-0002-7559-1090; Email: balu@zzu.edu.cn

Authors

Miao-Ying Chen – College of Materials Science and Engineering, Zhengzhou University, Zhengzhou 450001, P.R. China; State Key Laboratory of Physical Chemistry of Solid Surfaces, Department of Chemistry, College of Chemistry and Chemical Engineering, Xiamen University, Xiamen 361005, P.R. China; Shanghai Nanoport, Thermo Fisher Scientific, Shanghai 201206, P.R. China; Fujian Institute of Research on the Structure of Matter Chinese Academy of Sciences, Fuzhou 350002, P.R. China; State Key Laboratory of Inorganic Synthesis and Preparative Chemistry and College of Chemistry, Jilin University, Changchun 130012, P.R. China
Shuhu Yin – State Key Laboratory of Physical Chemistry of Solid Surfaces, Department of Chemistry, College of

Chemistry and Chemical Engineering, Xiamen University, Xiamen 361005, P.R. China

Gen Li – Shanghai Nanoport, Thermo Fisher Scientific, Shanghai 201206, P.R. China

Junxiang Chen – Fujian Institute of Research on the Structure of Matter Chinese Academy of Sciences, Fuzhou 350002, P.R. China

Wen-Yuan Zhao – College of Materials Science and Engineering, Zhengzhou University, Zhengzhou 450001, P.R. China

Yi-Kai Lian – College of Materials Science and Engineering, Zhengzhou University, Zhengzhou 450001, P.R. China;  orcid.org/0009-0007-0392-3379

Hao-Ran Wu – College of Materials Science and Engineering, Zhengzhou University, Zhengzhou 450001, P.R. China

Wenfu Yan – State Key Laboratory of Inorganic Synthesis and Preparative Chemistry and College of Chemistry, Jilin University, Changchun 130012, P.R. China;  orcid.org/0000-0002-1000-6559

Complete contact information is available at:

<https://pubs.acs.org/10.1021/acsnano.4c06615>

Author Contributions

#M.-Y.C. and S.Y. contributed equally. The manuscript was written through the contributions of all authors. All authors have given approval to the final version of the manuscript.

Notes

The authors declare no competing financial interest.

ACKNOWLEDGMENTS

This work was supported by the National Natural Science Foundation of China (No. 22102156, 22372152, and U22A20107), the China Postdoctoral Science Foundation (2021TQ0295 and 2022M712865), the Distinguished Young Scholars Innovation Team of Zhengzhou University (No. 32320275), and the Academic Degrees & Graduate Education Reform Project of Henan Province (2021 SJGLX 093Y).

REFERENCES

- (1) Zaman, S.; Huang, L.; Douka, A. I.; Yang, H.; You, B.; Xia, B. Y. Oxygen Reduction Electrocatalysts toward Practical Fuel Cells: Progress and Perspectives. *Angew. Chem., Int. Ed.* **2021**, *60*, 17832–17852.
- (2) Liang, J.; Ma, F.; Hwang, S.; Wang, X.; Sokolowski, J.; Li, Q.; Wu, G.; Su, D. Atomic Arrangement Engineering of Metallic Nanocrystals for Energy-Conversion Electrocatalysis. *Joule* **2019**, *3*, 956–991.
- (3) Lu, B.; Tian, N.; Sun, S. Surface Structure Effects of Platinum-Based Catalysts for Oxygen Reduction Reaction. *Curr. Opin. Electrochem.* **2017**, *4*, 76–82.
- (4) Wang, X. X.; Swihart, M. T.; Wu, G. Achievements, Challenges and Perspectives on Cathode Catalysts in Proton Exchange Membrane Fuel Cells for Transportation. *Nat. Catal.* **2019**, *2*, 578–589.
- (5) Chong, L.; Wen, J. G.; Kubal, J.; Sen, F. G.; Zou, J. X.; Greeley, J.; Chan, M.; Barkholtz, H.; Ding, W. J.; Liu, D. J. Ultralow-Loading Platinum-Cobalt Fuel Cell Catalysts Derived from Imidazolate Frameworks. *Science* **2018**, *362*, 1276–1281.
- (6) Xiao, F.; Wang, Q.; Xu, G.; Qin, X.; Hwang, I.; Sun, C.; Liu, M.; Hua, W.; Wu, H.-W.; Zhu, S.; et al. Atomically Dispersed Pt and Fe Sites and Pt-Fe Nanoparticles for Durable Proton Exchange Membrane Fuel Cells. *Nat. Catal.* **2022**, *5*, 503–512.
- (7) Luo, E.; Chu, Y.; Liu, J.; Shi, Z.; Zhu, S.; Gong, L.; Ge, J.; Choi, C. H.; Liu, C.; Xing, W. Pyrolyzed M-N_x Catalysts for Oxygen Reduction Reaction: Progress and Prospects. *Energy Environ. Sci.* **2021**, *14*, 2158–2185.
- (8) Adabi, H.; Shakouri, A.; Ul Hassan, N.; Varcoe, J. R.; Zulevi, B.; Serov, A.; Regalbuto, J. R.; Mustain, W. E. High-Performing Commercial Fe–N–C Cathode Electrocatalyst for Anion-Exchange Membrane Fuel Cells. *Nat. Energy* **2021**, *6*, 834–843.
- (9) Bouwkap-Wijnoltz, A. L.; Visscher, W.; van Veen, J. A. R.; Boellaard, E.; van der Kraan, A. M.; Tang, S. C. On Active-Site Heterogeneity in Pyrolyzed Carbon-Supported Iron Porphyrin Catalysts for the Electrochemical Reduction of Oxygen: An in situ Mössbauer Study. *J. Phys. Chem. B* **2002**, *106*, 12993–13001.
- (10) Kramm, U. I.; Herranz, J.; Larouche, N.; Arruda, T. M.; Lefevre, M.; Jaouen, F.; Bogdanoff, P.; Fiechter, S.; Abs-Wurmbach, I.; Mukerjee, S.; et al. Structure of the Catalytic Sites in Fe/N/C-Catalysts for O₂-Reduction in PEM Fuel Cells. *Phys. Chem. Chem. Phys.* **2012**, *14*, 11673–11688.
- (11) Luo, E.; Zhang, H.; Wang, X.; Gao, L.; Gong, L.; Zhao, T.; Jin, Z.; Ge, J.; Jiang, Z.; Liu, C.; et al. Single-Atom Cr–N₄ sites Designed for Durable Oxygen Reduction Catalysis in Acid Media. *Angew. Chem., Int. Ed.* **2019**, *58*, 12469–12475.
- (12) Wang, J.; Zhong, H.; Yang, J.; Li, H.; Tang, P.; Feng, Y.; Li, D. Tuning the Atomic Configuration Environment of MnN₄ Sites by Co Cooperation for Efficient Oxygen Reduction. *J. Energy Chem.* **2023**, *82*, 547–559.
- (13) Xie, X.; He, C.; Li, B.; He, Y.; Cullen, D. A.; Wegener, E. C.; Kropf, A. J.; Martinez, U.; Cheng, Y.; Engelhard, M. H.; et al. Performance Enhancement and Degradation Mechanism Identification of a Single-Atom Co–N–C Catalyst for Proton Exchange Membrane Fuel Cells. *Nat. Cata.* **2020**, *3*, 1044–1054.
- (14) Wu, H. R.; Chen, M. Y.; Li, W. D.; Lu, B. A. Recent Progress on Durable Metal-N-C Catalysts for Proton Exchange Membrane Fuel Cells. *Chem. Asian J.* **2024**, *19*, No. e202300862.
- (15) Shao, Y.; Dodelet, J. P.; Wu, G.; Zelenay, P. PGM-Free Cathode Catalysts for PEM Fuel Cells: a Mini-Review on Stability Challenges. *Adv. Mater.* **2019**, *31*, 1807615.
- (16) Tang, T.; Ding, L.; Jiang, Z.; Hu, J.-S.; Wan, L.-J. Advanced Transition Metal/Nitrogen/Carbon-Based Electrocatalysts for Fuel Cell Applications. *Sci. China: Chem.* **2020**, *63*, 1517–1542.
- (17) Choi, C. H.; Lim, H.-K.; Chung, M. W.; Chon, G.; Ranjbar Sahraie, N.; Altin, A.; Sougrati, M.-T.; Stievano, L.; Oh, H. S.; Park, E. S.; et al. The Achilles' Heel of Iron-Based Catalysts during Oxygen Reduction in an Acidic Medium. *Energy Environ. Sci.* **2018**, *11*, 3176–3182.
- (18) Ku, Y.; Ehelebe, K.; Hutzler, A.; Bierling, M.; Böhm, T.; Zitolo, A.; Vorokhta, M.; Bibent, N.; Speck, F. D.; Seeger, D.; et al. Oxygen Reduction Reaction in Alkaline Media Causes Iron Leaching from Fe–N–C Electrocatalysts. *J. Am. Chem. Soc.* **2022**, *144*, 9753–9763.
- (19) Choi, C. H.; Baldizzone, C.; Polymeros, G.; Pizzutilo, E.; Kasian, O.; Schuppert, A. K.; Ranjbar Sahraie, N.; Sougrati, M.-T.; Mayrhofer, K. J. J.; Jaouen, F. Minimizing Operando Demetallation of Fe-N-C Electrocatalysts in Acidic Medium. *ACS Catal.* **2016**, *6*, 3136–3146.
- (20) Gubler, L.; Dockheer, S. M.; Koppenol, W. H. Radical (HO[•], H[•] and HOO[•]) Formation and Ionomer Degradation in Polymer Electrolyte Fuel Cells. *J. Electrochem. Soc.* **2011**, *158*, B755–B769.
- (21) Ding, L.; Tang, T.; Hu, J.-S. Recent Progress in Proton-Exchange Membrane Fuel Cells Based on Metal-Nitrogen-Carbon Catalysts. *Acta Phys.-Chim. Sin.* **2020**, *0*, 2010048.
- (22) Qiu, C.; Gao, R.; Guo, Y.; Qin, J.; Zhang, G.; Song, Y. CeO₂ Nanoparticles Boosted Fe-N-C Sites Derived from Dual Metal Organic Frameworks toward Highly Active and Durable Oxygen Reduction Reaction. *Adv. Mater. Interfaces* **2022**, *9*, 2200852.
- (23) Wan, X.; Liu, Q.; Liu, J.; Liu, S.; Liu, X.; Zheng, L.; Shang, J.; Yu, R.; Shui, J. Iron atom–cluster interactions increase activity and improve durability in Fe–N–C fuel cells. *Nat. Commun.* **2022**, *13*, 2963.
- (24) Wei, H.; Su, X.; Liu, J.; Tian, J.; Wang, Z.; Sun, K.; Rui, Z.; Yang, W.; Zou, Z. A CeO₂ Modified Phenylenediamine-Based Fe/N/

- C with Enhanced Durability/Stability as Non-Precious Metal Catalyst for Oxygen Reduction Reaction. *Electrochem. Commun.* **2018**, *88*, 19–23.
- (25) Liao, W.; Zhou, S.; Wang, Z.; Long, J.; Chen, M.; Zhou, Q.; Wang, Q. Stress Induced to Shrink ZIF-8 Derived Hollow Fe-NC Supports Synergizes with Pt Nanoparticles to Promote Oxygen Reduction Electrocatalysis. *J. Mater. Chem. A* **2022**, *10*, 21416–21421.
- (26) Mechler, A. K.; Sahraie, N. R.; Armel, V.; Zitolo, A.; Sougrati, M. T.; Schwämmlein, J. N.; Jones, D. J.; Jaouen, F. Stabilization of Iron-Based Fuel Cell Catalysts by Non-Catalytic Platinum. *J. Electrochem. Soc.* **2018**, *165*, F1084–F1091.
- (27) Xiao, F.; Wang, Y.; Xu, G.; Yang, F.; Zhu, S.; Sun, C.; Cui, Y.; Xu, Z.; Zhao, Q.; Jang, J.; et al. Fe–N–C Boosts the Stability of Supported Platinum Nanoparticles for Fuel Cells. *J. Am. Chem. Soc.* **2022**, *144*, 20372–20384.
- (28) Zeng, Y.; Liang, J.; Li, B.; Yu, H.; Zhang, B.; Reeves, K. S.; Cullen, D. A.; Li, X.; Su, D.; Wang, G.; et al. Pt Nanoparticles on Atomic-Metal-Rich Carbon for Heavy-Duty Fuel Cell Catalysts: Durability Enhancement and Degradation Behavior in Membrane Electrode Assemblies. *ACS Catal.* **2023**, *13*, 11871–11882.
- (29) Zeng, Y.; Liang, J.; Li, C.; Qiao, Z.; Li, B.; Hwang, S.; Kariuki, N. N.; Chang, C.; Wang, M.; Lyons, M.; et al. Regulating Catalytic Properties and Thermal Stability of Pt and PtCo Intermetallic Fuel-Cell Catalysts via Strong Coupling Effects between Single-Metal Site-Rich Carbon and Pt. *J. Am. Chem. Soc.* **2023**, *145*, 17643–17655.
- (30) Yin, S.; Yan, Y.; Chen, L.; Cheng, N.; Cheng, X.; Huang, R.; Huang, H.; Zhang, B.; Jiang, Y.; Sun, S. FeN₄ Active Sites Electronically Coupled with PtFe Alloys for Ultralow Pt Loading Hybrid Electrocatalysts in Proton Exchange Membrane Fuel Cells. *ACS Nano* **2024**, *18*, 551–559.
- (31) Gao, X.; Wang, Y.; Xu, W.; Huang, H.; Zhao, K.; Ye, H.; Zhou, Z.; Zheng, N.; Sun, S. Mechanism of Particle-Mediated Inhibition of Demetalation for Single-Stom Catalytic Sites in Acidic Electrochemical Environments. *J. Am. Chem. Soc.* **2023**, *145*, 15528–15537.
- (32) Wei, X.; Song, S.; Cai, W.; Luo, X.; Jiao, L.; Fang, Q.; Wang, X.; Wu, N.; Luo, Z.; Wang, H.; et al. Tuning the Spin State of Fe Single Atoms by Pd Nanoclusters Enables Robust Oxygen Reduction with Dissociative Pathway. *Chem* **2023**, *9*, 181–197.
- (33) Borup, R.; Meyers, J.; Pivovar, B.; Kim, Y. S.; Mukundan, R.; Garland, N.; Myers, D.; Wilson, M.; Garzon, F.; Wood, D.; et al. Scientific Aspects of Polymer Electrolyte Fuel Cell Durability and Degradation. *Chem. Rev.* **2007**, *107*, 3904–3951.
- (34) Martinaou, I.; Shahraei, A.; Grimm, F.; Zhang, H.; Wittich, C.; Klemenz, S.; Dolique, S. J.; Kleebe, H.-J.; Stark, R. W.; Kramm, U. I. Effect of Metal Species on the Stability of Me-N-C Catalysts during Accelerated Stress Tests Mimicking the Start-Up and Shut-Down Conditions. *Electrochim. Acta* **2017**, *243*, 183–196.
- (35) Kim, J.; Lee, Y.; Sun, S. H. Structurally Ordered FePt Nanoparticles and Their Enhanced Catalysis for Oxygen Reduction Reaction. *J. Am. Chem. Soc.* **2010**, *132*, 4996–4997.
- (36) Li, J.; Sharma, S.; Liu, X.; Pan, Y.-T.; Spendelow, J. S.; Chi, M.; Jia, Y.; Zhang, P.; Cullen, D. A.; Xi, Z.; et al. Hard-Magnet L1₀-CoPt Nanoparticles Advance Fuel Cell Catalysis. *Joule* **2019**, *3*, 124–135.
- (37) Zhang, Q.; Shen, T.; Song, M.; Wang, S.; Zhang, J.; Huang, X.; Lu, S.; Wang, D. High-Entropy L1₂-Pt(FeCoNiCuZn)₃ Intermetallics for Ultrastable Oxygen Reduction Reaction. *J. Energy Chem.* **2023**, *86*, 158–166.
- (38) Wang, X.; Hwang, S.; Pan, Y.-T.; Chen, K.; He, Y.; Karakalos, S.; Zhang, H.; Spendelow, J. S.; Su, D.; Wu, G. Ordered Pt₃Co Intermetallic Nanoparticles Derived from Metal–Organic Frameworks for Oxygen Reduction. *Nano Lett.* **2018**, *18*, 4163–4171.
- (39) Song, T. W.; Chen, M. X.; Yin, P.; Tong, L.; Zuo, M.; Chu, S. Q.; Chen, P.; Liang, H. W. Intermetallic PtFe Electrocatalysts for the Oxygen Reduction Reaction: Ordering Degree-Dependent Performance. *Small* **2022**, *18*, 2202916.
- (40) Chen, J.; Dong, J.; Huo, J.; Li, C.; Du, L.; Cui, Z.; Liao, S. Ultrathin Co-N-C Layer Modified Pt–Co Intermetallic Nanoparticles Leading to a High-Performance Electrocatalyst toward Oxygen Reduction and Methanol Oxidation. *Small* **2023**, *19*, 2301337.
- (41) Nie, Y.; Chen, S.; Ding, W.; Xie, X.; Zhang, Y.; Wei, Z. Pt/C Trapped in Activated Graphitic Carbon Layers as a Highly Durable Electrocatalyst for the Oxygen Reduction Reaction. *Chem. Commun.* **2014**, *50*, 15431–15434.
- (42) Huang, L.; Su, Y.; Qi, R.; Dang, D.; Qin, Y.; Xi, S.; Zaman, S.; You, B.; Ding, S.; Xia, B. Y. Boosting Oxygen Reduction Via Integrated Construction and Synergistic Catalysis of Porous Platinum Alloy and Defective Graphitic Carbon. *Angew. Chem., Int. Ed.* **2021**, *60*, 25530–25537.
- (43) Hu, Y.; Lu, Y.; Zhao, X.; Shen, T.; Zhao, T.; Gong, M.; Chen, K.; Lai, C.; Zhang, J.; Xin, H. L.; et al. Highly Active N-Doped Carbon Encapsulated Pd-Fe Intermetallic Nanoparticles for the Oxygen Reduction Reaction. *Nano Res.* **2020**, *13*, 2365–2370.
- (44) Liu, D.; Zhang, J.; Liu, D.; Li, T.; Yan, Y.; Wei, X.; Yang, Y.; Yan, S.; Zou, Z. N-Doped Graphene-Coated Commercial Pt/C Catalysts toward High-Stability and Antipoisoning in Oxygen Reduction Reaction. *J. Phys. Chem. Lett.* **2022**, *13*, 2019–2026.
- (45) Yang, Q.; Jia, Y.; Wei, F.; Zhuang, L.; Yang, D.; Liu, J.; Wang, X.; Lin, S.; Yuan, P.; Yao, X. Understanding the Activity of Co-N_{4-x}C_x in Atomic Metal Catalysts for Oxygen Reduction Catalysis. *Angew. Chem., Int. Ed.* **2020**, *59*, 6122–6127.
- (46) Wang, C.; Chi, M.; Li, D.; Strmcnik, D.; van der Vliet, D.; Wang, G.; Komanicky, V.; Chang, K.-C.; Paulikas, A. P.; Tripkovic, D.; et al. Design and Synthesis of Bimetallic Electrocatalyst with Multilayered Pt-Skin Surfaces. *J. Am. Chem. Soc.* **2011**, *133*, 14396–14403.
- (47) Wang, D.; Xin, H. L.; Hovden, R.; Wang, H.; Yu, Y.; Muller, D. A.; DiSalvo, F. J.; Abruna, H. D. Structurally Ordered Intermetallic Platinum–Cobalt Core–Shell Nanoparticles with Enhanced Activity and Stability as Oxygen Reduction Electrocatalysts. *Nat. Mater.* **2013**, *12*, 81–87.
- (48) Ao, X.; Zhang, W.; Zhao, B.; Ding, Y.; Nam, G.; Soule, L.; Abdelhafiz, A.; Wang, C.; Liu, M. Atomically Dispersed Fe–N–C Decorated with Pt-Alloy Core–Shell Nanoparticles for Improved Activity and Durability towards Oxygen Reduction. *Energy Environ. Sci.* **2020**, *13*, 3032–3040.
- (49) Qiao, Z.; Wang, C.; Li, C.; Zeng, Y.; Hwang, S.; Li, B.; Karakalos, S.; Park, J.; Kropf, A. J.; Wegener, E. C.; et al. Atomically Dispersed Single Iron Sites for Promoting Pt and Pt₃Co Fuel Cell Catalysts: Performance and Durability Improvements. *Energy Environ. Sci.* **2021**, *14*, 4948–4960.
- (50) Song, T.; Xu, C.; Sheng, Z.; Yan, H.-K.; Tong, L.; Liu, J.; Zeng, W.; Zuo, L.; Yin, P.; Zuo, M.; Chu, S.; Chen, P.; Liang, H. Small Molecule-Assisted Synthesis of Carbon Supported Platinum Intermetallic Fuel Cell Catalysts. *Nat. Commun.* **2022**, *13*, 6521.
- (51) Deng, J.; Zhou, X.; Zou, J.; Qin, Y.; Wang, P. PdCo Alloy Supported on a ZIF-Derived N-Doped Carbon Hollow Polyhedron for Dehydrogenation of Ammonia Borane. *ACS Appl. Energy Mater.* **2022**, *5*, 7408–7419.
- (52) Jiang, Z.; Liu, X.; Liu, X.-Z.; Huang, S.; Liu, Y.; Yao, Z.-C.; Zhang, Y.; Zhang, Q.-H.; Gu, L.; Zheng, L.-R.; Li, L.; Zhang, J.; Fan, Y.; Tang, T.; Zhuang, Z.; Hu, J.-S. Interfacial Assembly of Binary Atomic Metal-N_x Sites for High-Performance Energy Devices. *Nat. Commun.* **2023**, *14*, 1822.
- (53) Stamenkovic, V. R.; Mun, B. S.; Arenz, M.; Mayrhofer, K. J. J.; Lucas, C. A.; Wang, G. F.; Ross, P. N.; Markovic, N. M. Trends in Electrocatalysis on Extended and Nanoscale Pt-Bimetallic Alloy Surfaces. *Nat. Mater.* **2007**, *6*, 241–247.
- (54) Luo, M. C.; Guo, S. J. Strain-Controlled Electrocatalysis on Multimetallic Nanomaterials. *Nat. Rev. Mater.* **2017**, *2*, 17059.
- (55) Mineva, T.; Matanovic, I.; Atanassov, P.; Sougrati, M.-T.; Stievano, L.; Clémancey, M.; Kochem, A.; Latour, J.-M.; Jaouen, F. Understanding Active Sites in Pyrolyzed Fe–N–C Catalysts for Fuel Cell Cathodes by Bridging Density Functional Theory Calculations and ⁵⁷Fe Mössbauer Spectroscopy. *ACS Catal.* **2019**, *9*, 9359–9371.
- (56) Xue, D.; Yuan, P.; Jiang, S.; Wei, Y.; Zhou, Y.; Dong, C.; Yan, W.; Mu, S.; Zhang, J. Altering the Spin State of Fe-N-C through Ligand Field Modulation of Single-Atom Sites Boosts the Oxygen Reduction Reaction. *Nano Energy* **2023**, *105*, 108020.

- (57) Zeng, Y.; Li, C.; Li, B.; Liang, J.; Zachman, M. J.; Cullen, D. A.; Hermann, R. P.; Alp, E. E.; Lavina, B.; Karakalos, S.; et al. Tuning the Thermal Activation Atmosphere Breaks the Activity–Stability Trade-Off of Fe–N–C Oxygen Reduction Fuel Cell Catalysts. *Nat. Catal.* **2023**, *6*, 1215–1227.
- (58) Yang, G.; Zhu, J.; Yuan, P.; Hu, Y.; Qu, G.; Lu, B.; Xue, X.; Yin, H.; Cheng, W.; Cheng, J.; Xu, W.; Li, J.; Hu, J.; Mu, S.; Zhang, J. Regulating Fe-Spin State by Atomically Dispersed Mn-N in Fe-N-C Catalysts with High Oxygen Reduction Activity. *Nat. Commun.* **2021**, *12*, 1734.
- (59) Wang, L.; Liu, B.; Su, C.; Liu, W.; Kei, C.; Wang, K.; Perng, T. Electronic Band Structure and Electrocatalytic Performance of Cu₃N Nanocrystals. *ACS Appl. Nano Mater.* **2018**, *1*, 3673–3681.
- (60) Lu, B.; Shen, L.; Liu, J.; Zhang, Q.; Wan, L.; Morris, D. J.; Wang, R.; Zhou, Z.; Li, G.; Sheng, T.; et al. Structurally Disordered Phosphorus-Doped Pt as a Highly Active Electrocatalyst for an Oxygen Reduction Reaction. *ACS Catal.* **2021**, *11*, 355–363.
- (61) Fan, A.; Qin, C.; Zhao, R.; Sun, H.; Sun, H.; Dai, X.; Ye, J.; Sun, S.; Lu, Y.; Zhang, X. Phosphorus-Doping-Tuned PtNi Concave Nanocubes with High-Index Facets for Enhanced Methanol Oxidation Reaction. *Nano Res.* **2022**, *15*, 6961–6968.
- (62) Sung, S. S.; Hoffmann, R. How Carbon Monoxide Bonds to Metal Surfaces. *J. Am. Chem. Soc.* **1985**, *107*, 578–584.
- (63) Blyholder, G. Molecular Orbital View of Chemisorbed Carbon Monoxide. *J. Phys. Chem.* **1964**, *68*, 2772–2777.
- (64) Baxter, R. J.; Hu, P. Insight into Why the Langmuir–Hinshelwood Mechanism is Generally Preferred. *J. Chem. Phys.* **2002**, *116*, 4379–4381.
- (65) Razdan, N. K.; Bhan, A. Catalytic Site Ensembles: A Context to Reexamine the Langmuir–Hinshelwood Kinetic Description. *J. Catal.* **2021**, *404*, 726–744.
- (66) Wang, Y.; Seo, B.; Wang, B.; Zamel, N.; Jiao, K.; Adroher, X. C. F. Fundamentals, Materials, and Machine Learning of Polymer Electrolyte Membrane Fuel Cell Technology. *Energy And AI* **2020**, *1*, 100014.
- (67) Bae, G.; Chung, M. W.; Ji, S. G.; Jaouen, F.; Choi, C. H. pH Effect on the H₂O₂-Induced Deactivation of Fe-N-C Catalysts. *ACS Catal.* **2020**, *10*, 8485–8495.

Supporting Information

Strong Electronic Metal-Support Interactions Enable the Increased Spin State of Co-N₄ Active Sites and Performance for Acidic Oxygen Reduction Reaction

Miao-Ying Chen,^{‡, a} Shuhu Yin,^{‡, b} Gen Li,^c Junxiang Chen,^d Wen-Yuan Zhao^a Yi-Kai Lian,^a Hao-Ran Wu,^a Wenfu Yan,^e Jia-Nan Zhang,^{ a} Bang-An Lu^{* a}*

^aCollege of Materials Science and Engineering, Zhengzhou University, Zhengzhou 450001, P. R. China

^bState Key Laboratory of Physical Chemistry of Solid Surfaces, Department of Chemistry, College of Chemistry and Chemical Engineering, Xiamen University, Xiamen 361005, P. R. China

^cShanghai Nanoport, Thermo Fisher Scientific, Shanghai, P. R. China

^dFujian Institute of Research on the Structure of Matter Chinese Academy of Sciences, Fuzhou, 350002, P. R. China

^eState Key Laboratory of Inorganic Synthesis and Preparative Chemistry and College
of Chemistry, Jilin University, Changchun 130012, P. R. China

[‡]Miao-Ying Chen and [‡]Shuhu Yin contributed equally.

*Corresponding authors:

balu@zzu.edu.cn (Prof. Bang-An Lu) and zjn@zzu.edu.cn (Prof. Jia-Nan Zhang)

1. Data analysis

EXAFS data analysis. The acquired EXAFS data were processed according to the standard procedures using the ATHENA module implemented in the IFEFFIT software packages. The EXAFS spectra were obtained by subtracting the post-edge background from the overall absorption and then normalizing with respect to the edge-jump step. Subsequently, Data of Co K-edge (Pt L₃-edge) were Fourier transformed to real (R) space using a hanning windows ($dk=1.0 \text{ \AA}^{-1}$) to separate the EXAFS contributions from different coordination shells. To obtain the quantitative structural parameters around central atoms, least-squares curve parameter fitting was performed using the ARTEMIS module of IFEFFIT software packages.

UPS data analysis. The work function (ϕ) can be calculated by the following equation:

$$\phi = 21.22 \text{ eV} - E_{\text{cutoff}} \quad (\text{Equation S1})$$

where h is Planck constant, v is the frequency of the He I excitation light source, and the product of hv (21.22 eV) represents the incident light energy from the He I excitation source, and E_{cutoff} is the cutoff edge of the secondary electron.

VSM data analysis. The effective magnetic moment (μ_{eff}) correlates with the number of unpaired electron (n) of Co ion via the following equation:

$$2.828\sqrt{\chi_m T} = \mu_{\text{eff}} = \sqrt{n(n+2)} \quad (\text{Equation S2})$$

where T is the Curie temperature, χ_m the magnetization intensity M corresponds to the Curie temperature point in the M-T curve divided by the magnetic field intensity H .

2. Electrochemical tests

Rotating disk electrode (RDE) test. The electrochemical experiments were performed on a CHI Electrochemical Station (Model 760e) using a three-electrode system, with the RDE serving as the working electrode, the carbon rod as the counter electrode, and the saturated calomel electrode as the reference electrode. All reference potentials have been converted to a reversible hydrogen electrode (RHE).

Prepare the working electrode, the homogeneous catalyst ink was prepared by sonicating the mixture of 2 mg of catalyst, 660 μL of IPA, 330 μL deionized water, and 10 μL of Nafion solution (5 wt%) for 20 min. A thin film catalyst layer ($200 \mu\text{g}_{\text{catalyst}}$ cm^{-2}) was obtained by depositing 20 μL of catalyst ink onto the RDE (0.196 cm^{-2}). Before the experiments, N_2 was bubbled for at least 30 minutes to ensure that the electrolyte was saturated by N_2 . Then, cyclic voltammetry (CV) was performed to activate the catalysts completely. After that, RDE tests were conducted at 1600 rpm in O_2 -saturated 0.1 M HClO_4 electrolyte.

The 20 wt% JM Pt/C catalyst was used as a benchmark at a loading of $100 \mu\text{g}_{\text{catalyst}}$ cm^{-2} ($4 \mu\text{g}_{\text{Pt}}$).

Rotating ring disk electrode (RRDE) test. During the ORR process, the H₂O₂ intermediate would diffuse from the disk electrode to the Pt ring. The potential of the Pt ring was set to 1.2 V vs. RHE so that the diffused H₂O₂ could be oxidized instantly at the Pt ring electrode. The peroxide yields (H₂O₂%) were calculated from the ring current (I_r) and the disk current (I_d) using the following equation:

$$\text{H}_2\text{O}_2\% = \frac{200 \times I_r}{(I_r + N \times I_d)} \quad (\text{Equation S3})$$

where N=0.37 is the current collection efficiency of the Pt ring.

From the Koutecky-Levich (K-L) equation, we can get the kinetic current density i_K .

$$\frac{1}{i} = \frac{1}{i_L} + \frac{1}{i_K} \quad (\text{Equation S4})$$

where i is the current density from practical measurements, i_L and i_K are the diffusion-limited current density and the kinetic current density, respectively.

Accelerated durability test (ADT). To evaluate the electrochemical stability of the catalysts, the stability test was carried out in O₂-saturated 0.1 M HClO₄ electrolyte, with a potential range of 0.6-1.0 V and sweep speed of 100 mV s⁻¹.

ADT for inductively coupled plasma mass spectrometry (ICP-MS). The electrolyte used for ICP-MS is collected from a simple electrochemical cell, as shown in **Figure S39**. The working electrode is a rotating disk electrode with a glassy carbon tip, a carbon rod as the counter electrode, and the reference electrode is a saturated calomel electrode. The catalyst loading is 40 µg on the glassy carbon tip. The electrolyte is 100

ml O₂-saturated 0.1 M HClO₄. The electrochemical testing conditions follow the ADT mentioned above. The electrolyte is kept being bubbled by O₂ during ADT.

3. Density functional theory (DFT) calculation

3. 1. Details of the simulation of the interface

In this study, we aim to construct models for the L1₂-Pt₃Co/Co-N-C and Co-N-C interphases. It is important to emphasize that the formation of interfaces between two phases is diverse and amorphous. The lattice within each phase may not necessarily undergo changes. Therefore, it is unreasonable to attempt to simulate interface reactions by establishing a regular interface model through minimal lattice deformation adaptation, as commonly seen in general literature. Instead, our modeling approach involves constructing larger models (approximately 3 nm in size, with around 2000 atoms) and then obtaining accurate interface configurations by placing clusters or larger particles and optimizing their structures. To accomplish structure optimization at this scale, we utilized force fields based on DFT-derived machine learning potentials (MLP).^[1]

The particulars of this methodology are delineated as follows:

DFT data used for MLP generation. We employ the configurations illustrated in **Figure S36** as the basis for training our force field. These structures are considered to possess characteristic features of Co-N-C, Pt/Co-N-C, L1₂-Pt₃Co/C, and L1₂-Pt₃Co/Co-

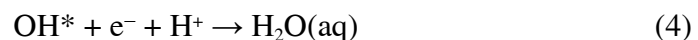
N-C structures. Commencing from these initial structures, we embark on a series of ab initio molecular dynamics (AIMD) simulations spanning a duration of 0.7 ps, during which temperatures are systematically varied from 1000 to 300 K. The integration of these simulations is facilitated by a time step of 1 fs. The resultant AIMD data, inclusive of atomic forces, energies, and local atomic environments, is harnessed in the construction of our machine learning potential, which is rooted in DFT principles. After that, we execute a DPGEN likeloop to finetune the force field.^[2]

Molecular dynamics details. To obtain more accurate structures, after acquiring the force field, we employed an annealing simulation approach for these four samples. The annealing temperature was set from 1500 to 300 K, with temperature control using the Nose-Hoover Thermostat, adjusting the temperature every 100 K steps. The simulation time step was 1 fs, with a total simulation duration of 200 ps. During the simulation, considering the system as an intermetallic compound, we enforced a temperature of 10 K within 2 nm of the PtCo and Pt particles internally to maintain the coordination and crystal structure of the intermetallic compound. All the annealing simulations are executed utilizing the extensive capabilities of the large-scale atomic/molecular massively parallel simulator (LAMMPS), the process is shown in *.mp4.^[3]

3. 2. Details for ORR calculation

Model construction. Given the substantial scale of the system under investigation, direct DFT calculations become impractical. To circumvent this limitation, we adopted a judicious model-cutting strategy. In this approach, for the extensive computational sites, we used a cutoff radius of 5 Å, where atoms within 3-5 Å of the reaction center were fixed to prevent structural collapse. Notably, for the three structures mentioned in the main text, we employed higher precision, using a 9 Å cutoff radius, and ensured that atoms within 4-9 Å of the reaction center were fixed.

The approach to study the ORR activity study. The activity of ORR is calculated based on the following mechanism:



The computational hydrogen electrode (CHE) method was introduced to deal with the charged species, including H^+ and e^- .^[4] The chemical potential for associated adsorbates were calculated via the following expressions:

$$\mu_A = E_A + ZPE - TS \quad (\text{Equation S5})$$

E_A is the total energy of a certain molecule A or adsorbate ${}^*\text{A}$. For molecule, E_A can be obtained directly through a gas phase calculation; for a certain adsorbate, E_{A}^* is

calculated by the difference between the DFT based substrate with ($E_{\text{A}}^{\text{DFT}}$) and without adsorbate A (E^{DFT}):

$$E_{\text{A}} = E_{\text{A}}^{\text{DFT}} - E^{\text{DFT}} \quad (\text{Equation S6})$$

ZPE and TS are the correction from zero-point energy and, entropy, whose values are listed on **Table S8**.

3. 3. DFT, and ML parameters

Spin-polarized DFT calculations were meticulously conducted within periodic supercells, employing the generalized gradient approximation (GGA) alongside the Perdew-Burke-Ernzerhof (PBE) functional for exchange-correlation. The expansion of Kohn-Sham orbitals transpired within a plane-wave basis set, characterized by a kinetic energy cutoff of 30 Ry and a charge-density cutoff of 300 Ry. Notably, the point of marginal adsorption energy change resides beyond these values, exhibiting variations within a scant 0.02 eV range. To account for Fermi-surface effects, we judiciously employed the smearing technique introduced by Methfessel and Paxton, leveraging a smearing parameter of 0.02 Ry. Convergence criteria were judiciously established, entailing Cartesian force components acting on each atom to reach a precision of 10^{-3} Ry/Bohr, and a total energy convergence threshold of 10^{-5} Ry. In alignment with the non-periodic nature of molecules, a gamma k-point mesh was uniformly employed to sample the Brillouin zones. To further enhance accuracy, the dispersion correction was

consistently incorporated across all calculations, employing the semiempirical zero damping D3 method advanced by Grimme.^[5] All the calculations were conducted by the PWSCF codes contained in the Quantum ESPRESSO distribution.^[6]

All the MLP were generated by DeePMD-kit package.^[7] The implemented codes establish a high-dimensional neural network framework that upholds the inherent symmetries present within the structural analysis. Simultaneously, they efficiently replicate indistinguishable features in alignment with the DFT-derived data, resulting in a compact representation of the force field. During the learning phase, a cut-off radius of 5 Å is employed, encompassing a maximum of 80 neighboring atoms treated via full relative coordinates for all atoms. Smoothing procedures are initiated from a fractional interval of 1/5 and extend to 2. The embedding nets consist of hidden layers with neuron counts of 10, 20, and 40, while the fitting net is composed of hidden layers with neuron counts of 240, 240, and 240. Initiation of the training process involves setting the only force loss. The learning rate at the outset is established at 0.001, with a decay step of 1000 and a decay rate of 0.95. The choice of the loss function is contingent upon the specific context, determined by whether it pertains to atomic energy or a combination of force and atomic energy components. Ultimately, the 732,538 data points used are presented in **Figure S36**. The RMSE of energy and force are as small as 57 m eV atom⁻¹ and 0.287 eV Å⁻¹, respectively.

4. Supplementary Figures

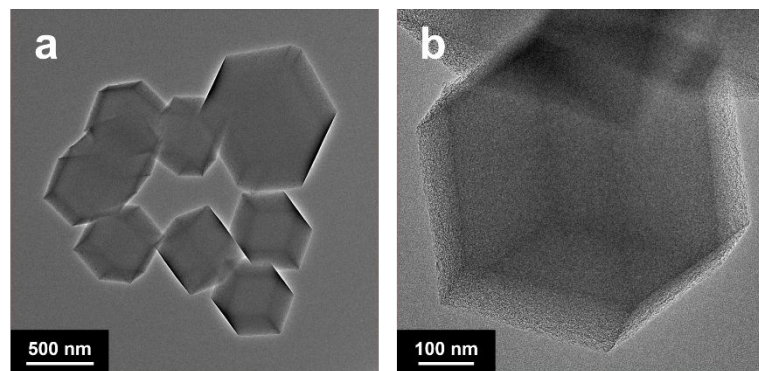


Figure S1. TEM images of different scale bar (a) 500 nm and (b) 100 nm for Co-N-C.

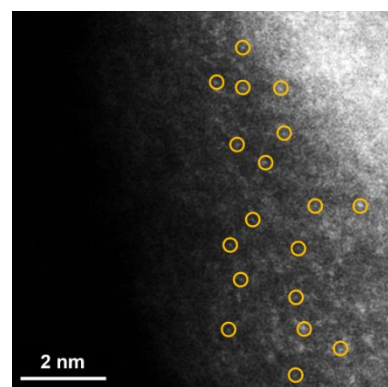


Figure S2. AC-HAADF-STEM image of Co-N-C.

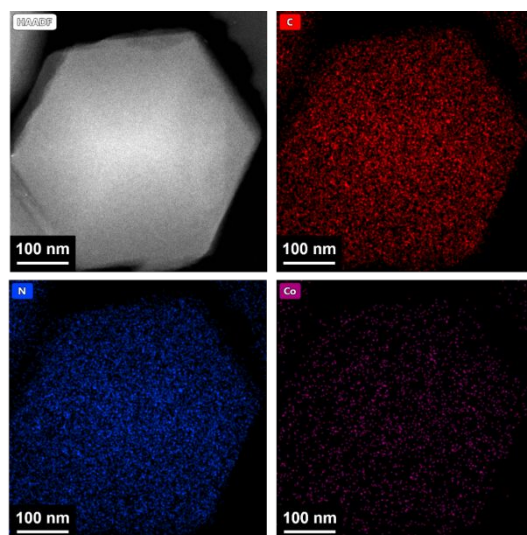


Figure S3. TEM image and relevant EDS elemental mappings of C, N, and Co for Co-

N-C.

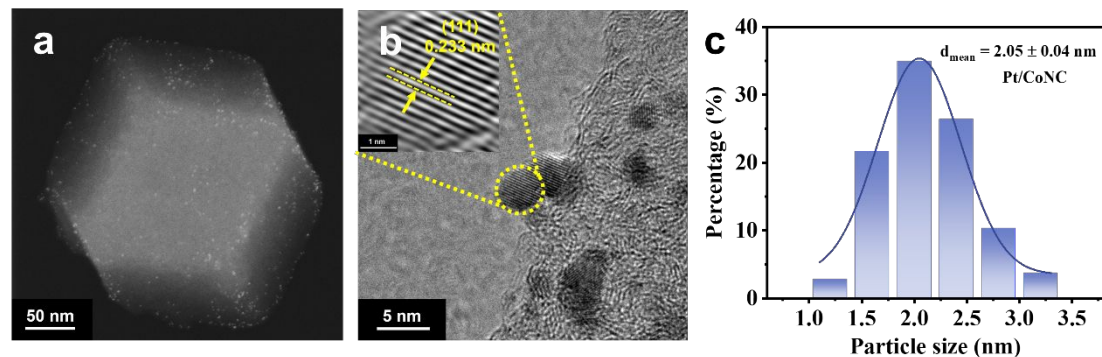


Figure S4. (a) TEM image, (b) HRTEM image, and (c) size distribution of Pt particles for Pt/Co-N-C.

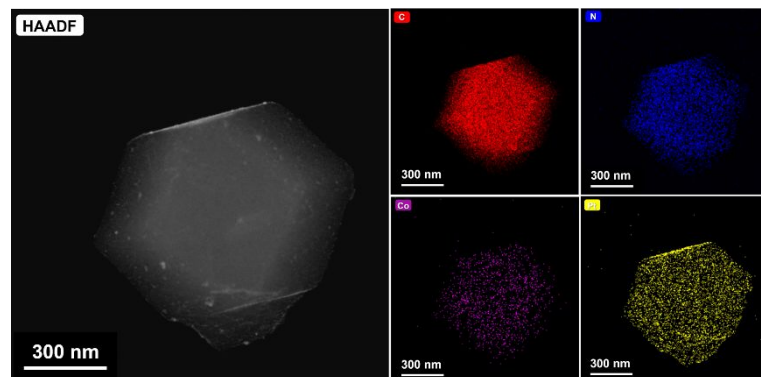


Figure S5. (a) TEM image and relevant EDS elemental mappings of N, C, Co, and Pt for Pt/Co-N-C.

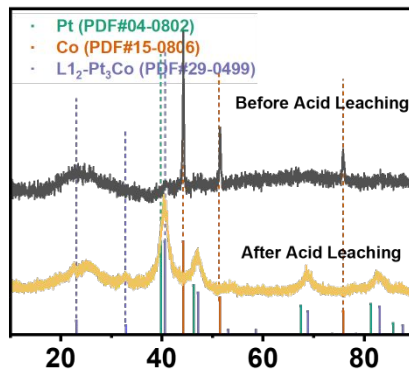


Figure S6. XRD patterns of L₁₂-Pt₃Co/Co-N-C before and after acid washing.

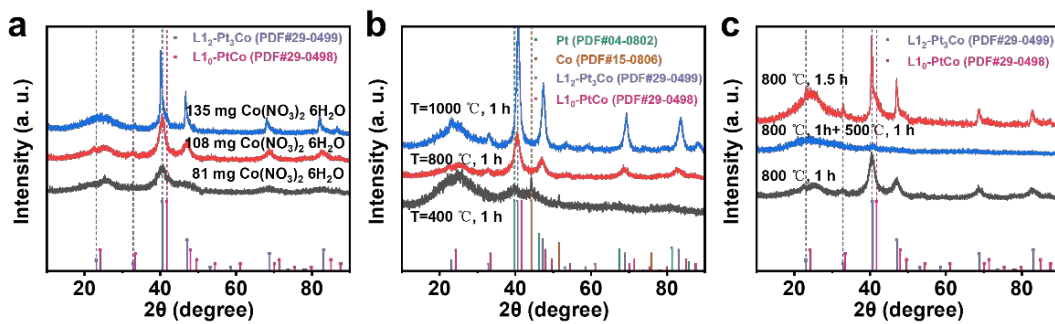


Figure S7. (a) XRD patterns of samples with different Co content. Temperature: 800 °C; Holding time: 1 h. (b) XRD patterns of samples with different heat treatment temperatures. Co content: 108 mg; Holding time: 1 h. (c) XRD patterns of samples with different holding conditions.

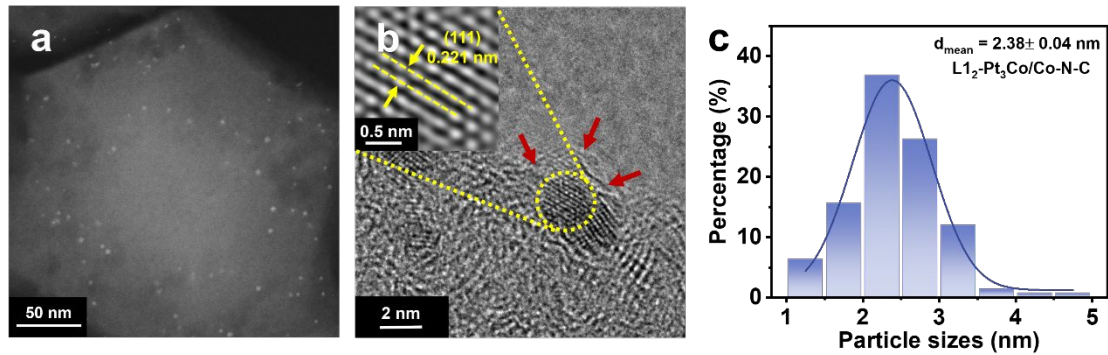


Figure S8. (a) TEM image, (b) HRTEM image, and (c) size distribution of Pt₃Co particles for L₁₂-Pt₃Co/Co-N-C.

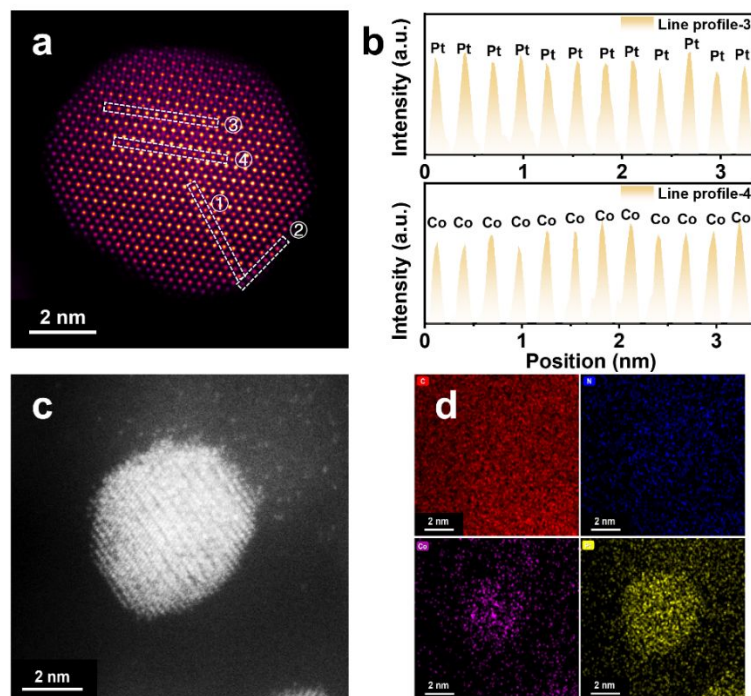


Figure S9. (a) AC-HAADF-STEM image of L₁₂-Pt₃Co NP within L₁₂-Pt₃Co/Co-N-C. (b) Line scan profiles corresponding to the white box in (a). (c) HAADF-STEM image and (d) relevant EDS elemental mappings of N, C, Co, and Pt for L₁₂-Pt₃Co/Co-N-C.

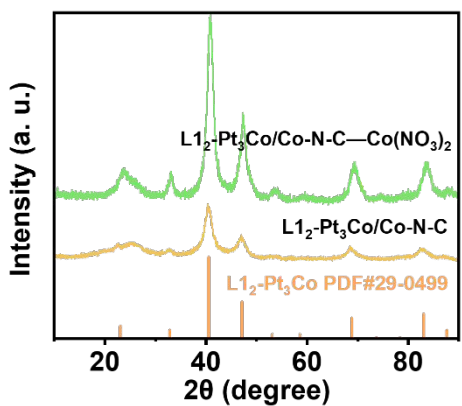


Figure S10. XRD patterns of $\text{L1}_2\text{-Pt}_3\text{Co/Co-N-C}$ and $\text{L1}_2\text{-Pt}_3\text{Co/Co-N-C--Co}(\text{NO}_3)_2$.

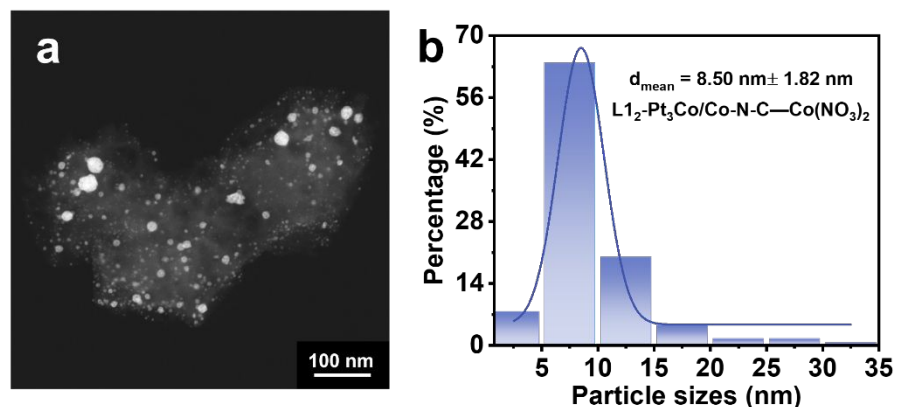


Figure S11. (a) TEM image and (b) size distribution of Pt_3Co particles for $\text{L1}_2\text{-Pt}_3\text{Co/Co-N-C--Co}(\text{NO}_3)_2$.

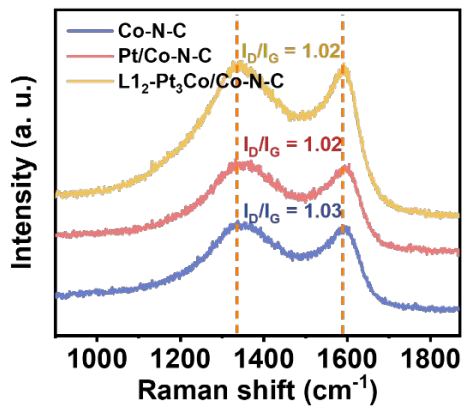


Figure S12. Raman spectra of Co-N-C, Pt/Co-N-C, and L₁₂-Pt₃Co/Co-N-C.

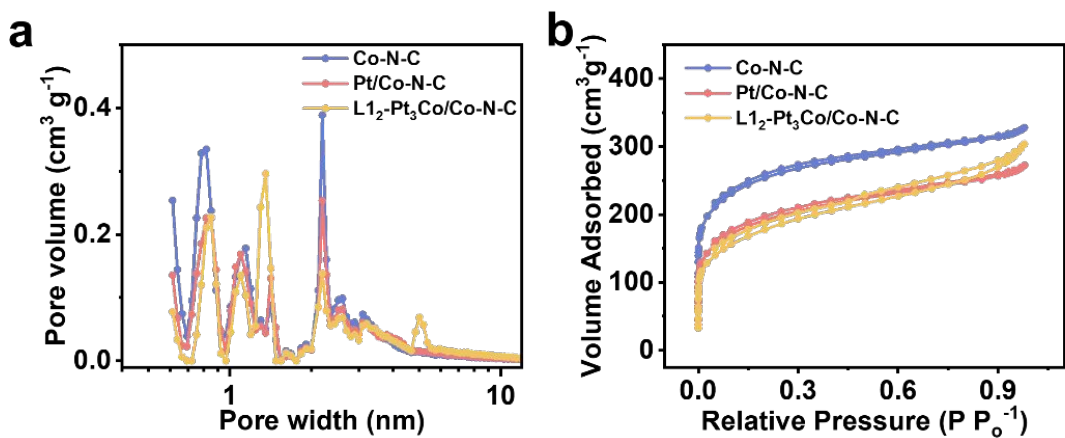


Figure S13. (a) Pore size distribution for Co-N-C, Pt/Co-N-C, and L₁₂-Pt₃Co/Co-N-C

from non-local density functional theory (NLDFT) model of the N₂ adsorption data.

(b) N₂ adsorption/desorption isotherms of Co-N-C, Pt/Co-N-C, and L₁₂-Pt₃Co/Co-N-

C.

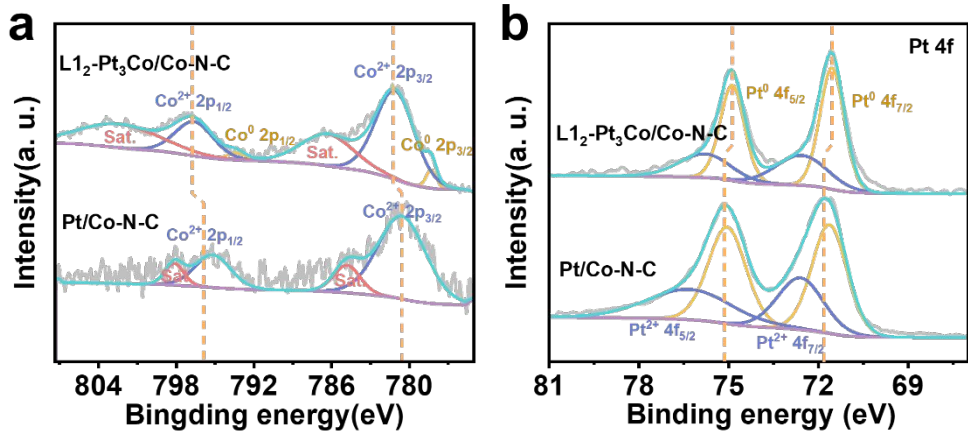


Figure S14. (a) Co 2p XPS fine spectra of Pt/Co-N-C and L₁₂-Pt₃Co/Co-N-C. (b) Pt 4f XPS fine spectra of Pt/Co-N-C and L₁₂-Pt₃Co/Co-N-C.

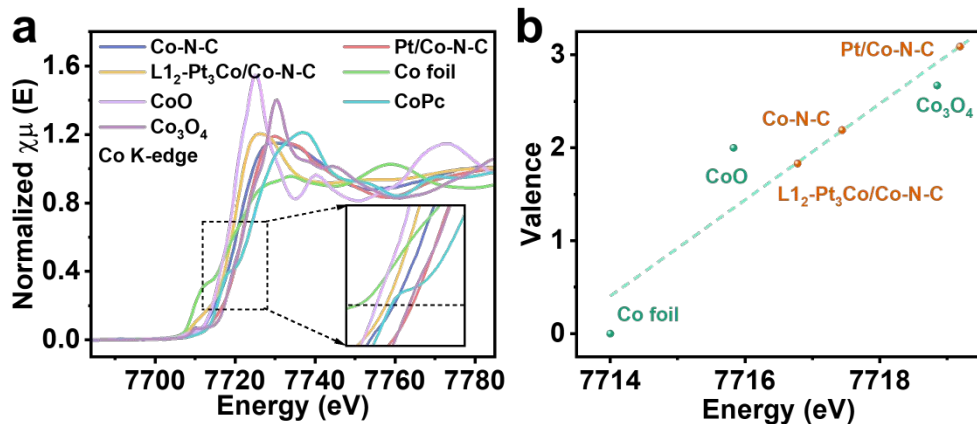


Figure S15. (a) Normalized Co K-edge XANES spectra of Co-N-C, Pt/Co-N-C, L₁₂-Pt₃Co/Co-N-C, and reference samples. (b) The average valence of Co in Co-N-C, Pt/Co-N-C, and L₁₂-Pt₃Co/Co-N-C.

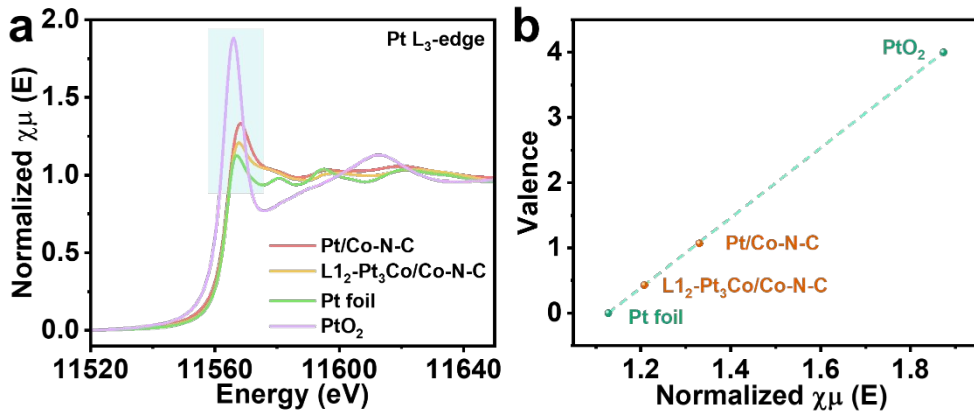


Figure S16. (a) Normalized Pt L₃-edge XANES spectra of Pt/Co-N-C, L₁₂-Pt₃Co/Co-N-C, and reference samples. (b) The average valence of Pt in Pt/Co-N-C and L₁₂-Pt₃Co/Co-N-C.

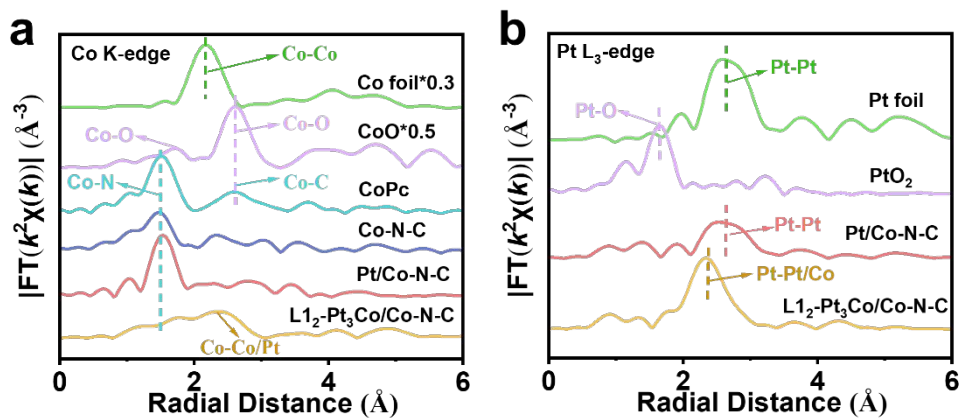


Figure S17. FT-EXAFS spectra of (a) Co K-edge and (b) Pt L₃-edge for Co-N-C, Pt/Co-N-C, and L₁₂-Pt₃Co/Co-N-C.

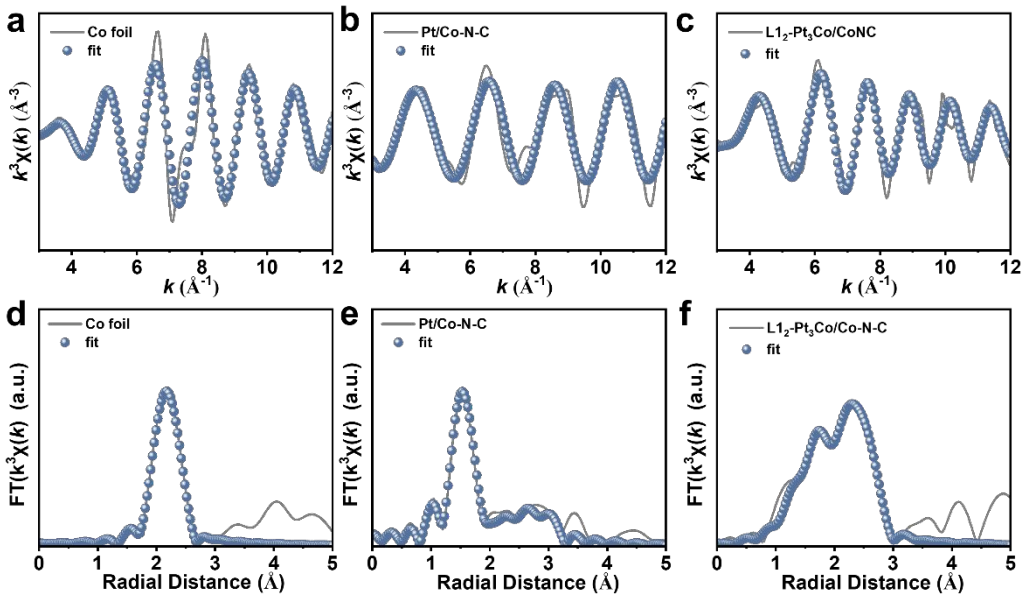


Figure S18. FT-EXAFS and corresponding EXAFS fitting curves of Co K-edge for (a, d) Co foil, (b, e) Pt/Co-N-C, and (c, f) L₁₂-Pt₃Co/Co-N-C in the k space and R space.

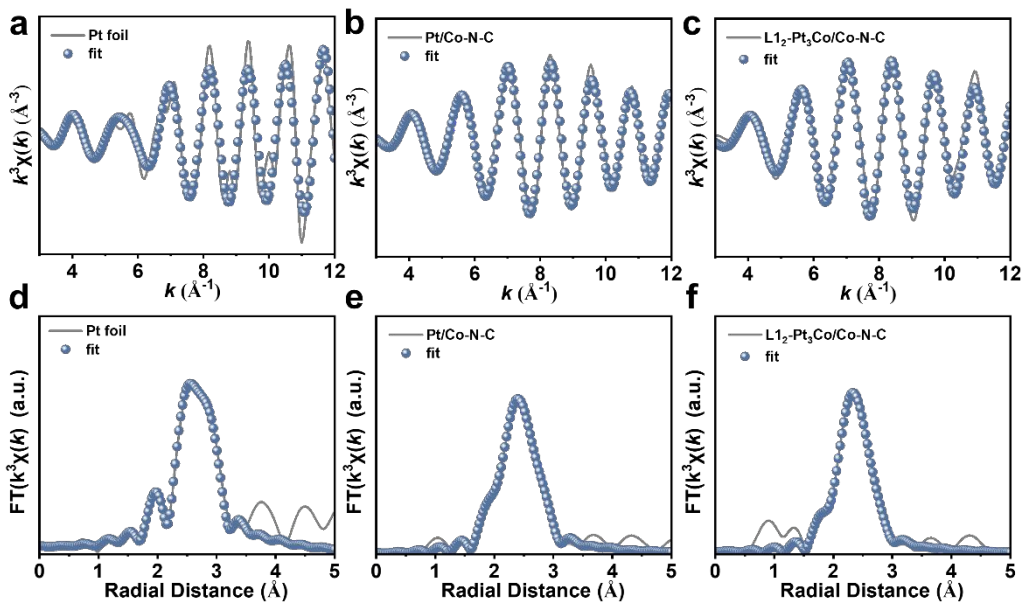


Figure S19. FT-EXAFS and corresponding EXAFS fitting curves of Pt L₃-edge for (a, d) Pt foil, (b, e) Pt/Co-N-C, and (c, f) L₁₂-Pt₃Co/Co-N-C in the k space and R space.

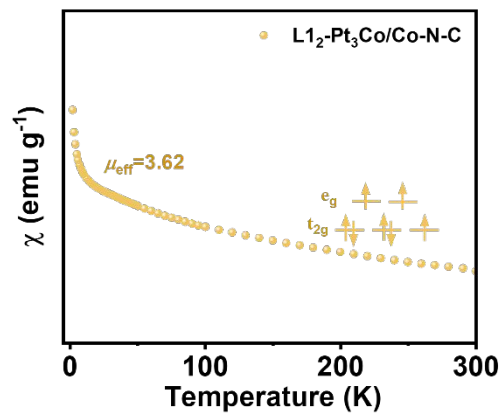


Figure S20. Magnetic susceptibility of $\text{L1}_2\text{-Pt}_3\text{Co/Co-N-C}$.

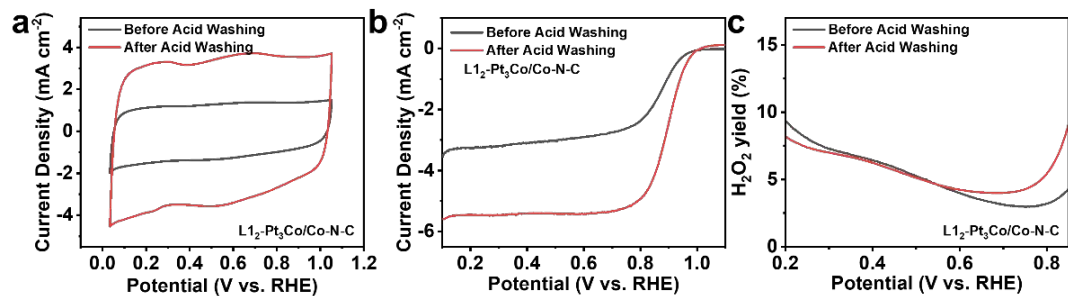


Figure R21 (a) CV curves, (b) ORR polarization curves, and (c) H_2O_2 yield of $\text{L1}_2\text{-Pt}_3\text{Co/Co-N-C}$ before and after acid washing in 0.1 M HClO_4 .

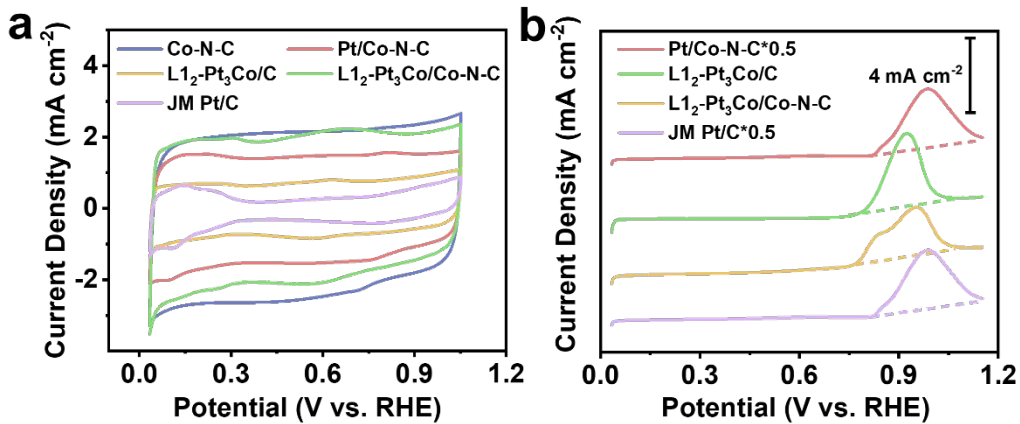


Figure S22. (a) CV curves of Co-N-C, Pt/Co-N-C, L₁₂-Pt₃Co/C, L₁₂-Pt₃Co/Co-N-C, and JM Pt/C in N₂-saturated 0.1 M HClO₄ with a scanning rate of 50 mV s⁻¹ and rotation rate of 1600 rpm. (b) CO-stripping curves of Pt/Co-N-C, L₁₂-Pt₃Co/C, L₁₂-Pt₃Co/Co-N-C, and JM Pt/C in N₂-saturated 0.1 M HClO₄ with a scanning rate of 50 mV s⁻¹.

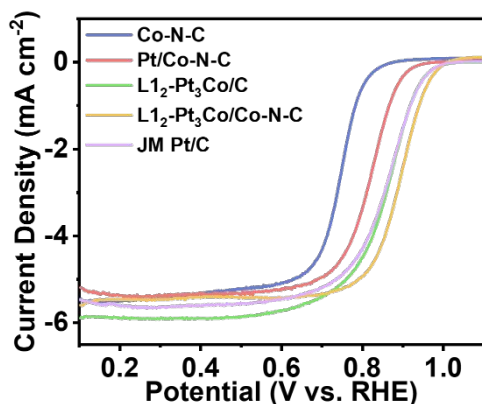


Figure S23. The ORR polarization curves of Co-N-C, Pt/Co-N-C, L₁₂-Pt₃Co/C, L₁₂-Pt₃Co/Co-N-C, and JM Pt/C in O₂-saturated 0.1 M HClO₄ with a scanning rate of 10 mV s⁻¹ and rotation rate of 1600 rpm.

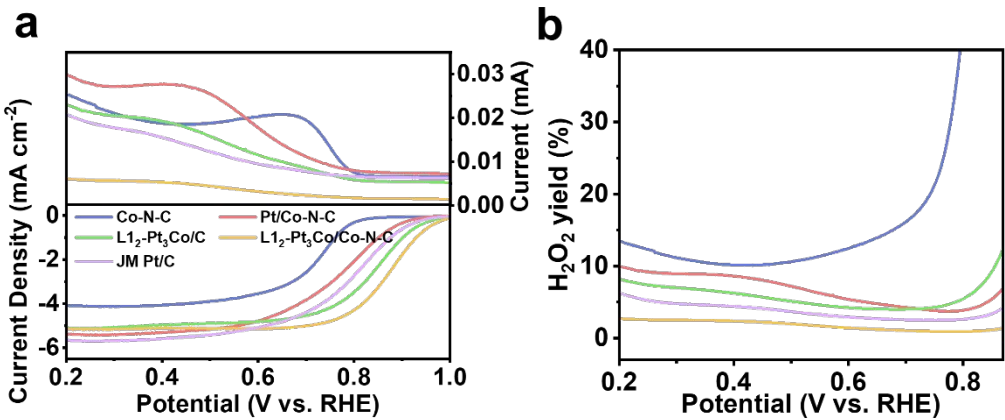


Figure S24. (a) The ring and disk current and (b) H_2O_2 yield of Co-N-C, Pt/Co-N-C, L₁₂-Pt₃Co/C, L₁₂-Pt₃Co/Co-N-C, and JM Pt/C in O_2 -saturated 0.1 M HClO_4 . The potential scanning rate is 10 mV s⁻¹ and the rotation rate is 1600 rpm.

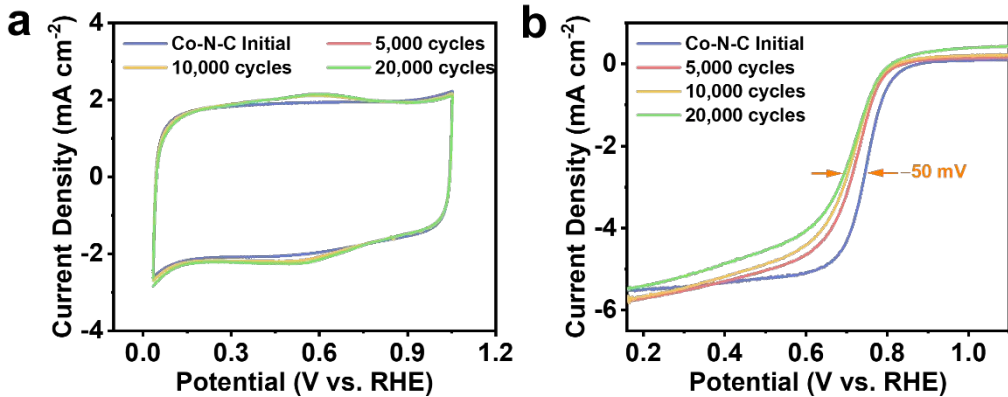


Figure S25 (a) CV curves of Co-N-C in N_2 -saturated 0.1 M HClO_4 before and after ADT at room temperature (RT). (b) ORR polarization curves of Co-N-C in O_2 -saturated 0.1 M HClO_4 before and after ADT at RT. (200 $\mu\text{g}_{\text{catalyst}} \text{cm}^{-2}$)

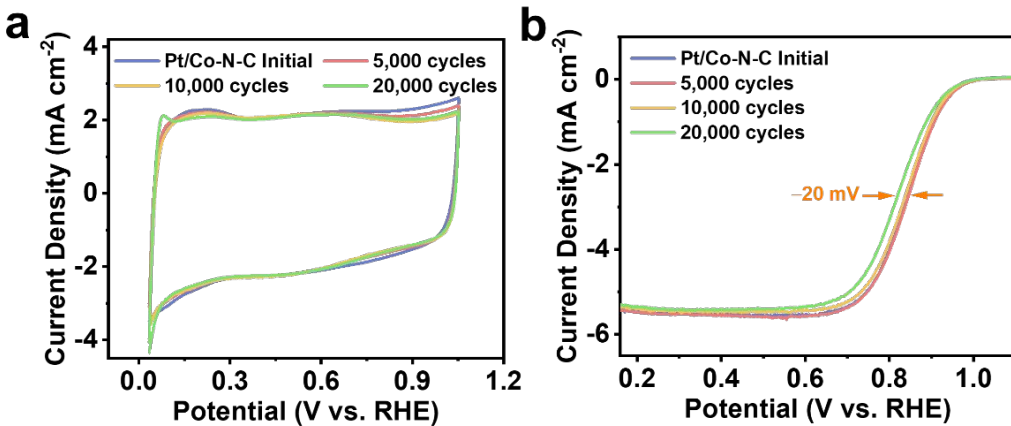


Figure S26. (a) CV curves of Pt/Co-N-C in N_2 -saturated 0.1 M HClO_4 before and after ADT at RT. (b) ORR polarization curves of Pt/Co-N-C in O_2 -saturated 0.1 M HClO_4 before and after ADT at RT. ($9.07 \mu\text{g}_{\text{Pt}} \text{cm}^{-2}$)

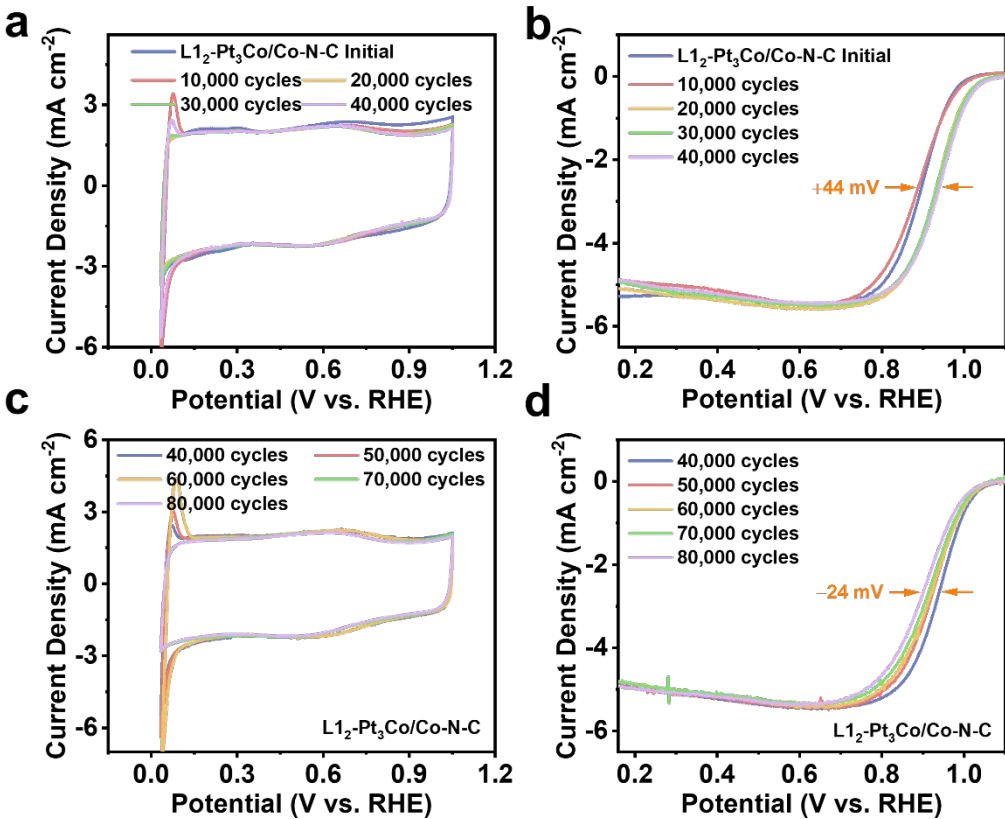


Figure S27. (a, c) CV curves of L₁₂-Pt₃Co/Co-N-C in N_2 -saturated 0.1 M HClO_4

before and after ADT at RT. (b, d) ORR polarization curves of L₁₂-Pt₃Co/Co-N-C in O₂-saturated 0.1 M HClO₄ before and after ADT at RT. (3.44 μg_{Pt} cm⁻²)

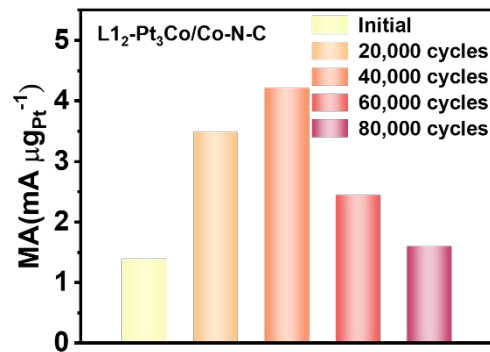


Figure S28. MA of L₁₂-Pt₃Co/Co-N-C after ADT at RT in O₂-saturated 0.1 M HClO₄.

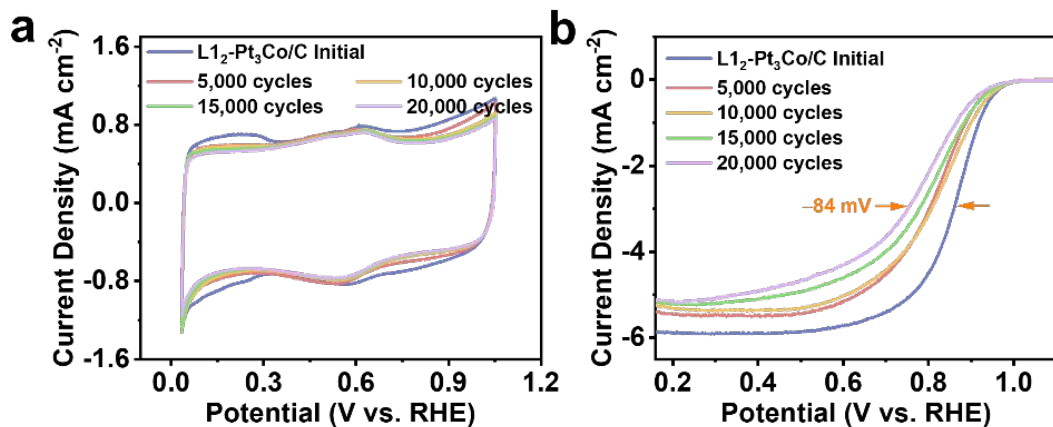


Figure S29. (a) CV curves of L₁₂-Pt₃Co/C in N₂-saturated 0.1 M HClO₄ before and after ADT at RT. (b) ORR polarization curves of L₁₂-Pt₃Co/C in O₂-saturated 0.1 M HClO₄ before and after ADT at RT. (3.44 μg_{Pt} cm⁻²)

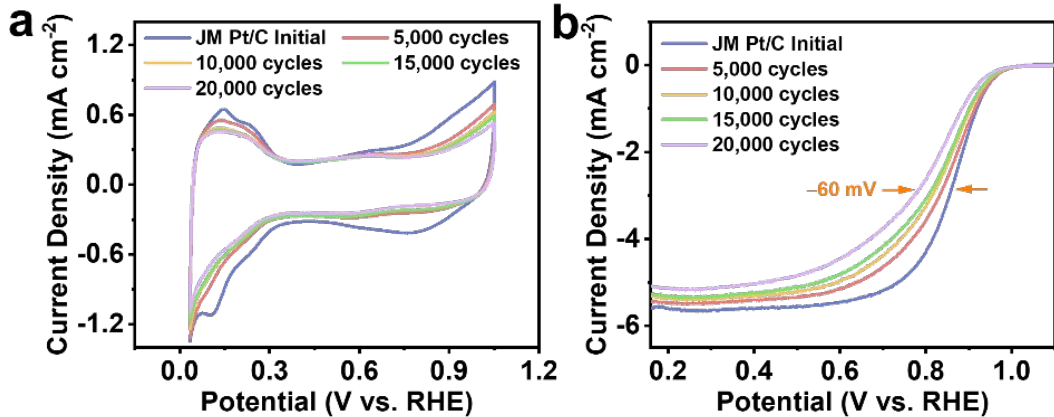


Figure S30. (a) CV curves of JM Pt/C in N_2 -saturated 0.1 M HClO_4 before and after ADT at RT. (b) ORR polarization curves of JM Pt/C in O_2 -saturated 0.1 M HClO_4 before and after ADT at RT. ($20 \mu\text{g}_{\text{Pt}} \text{cm}^{-2}$)

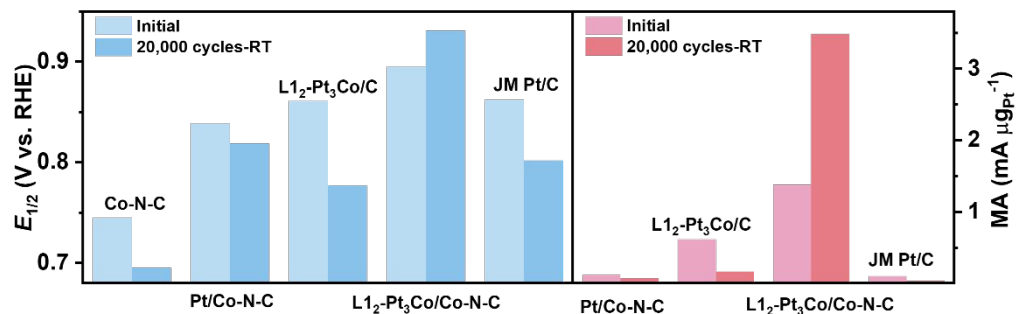


Figure S31. $E_{1/2}$, MA (@0.9 V), and SA (@0.9 V) values for the studied catalysts before and after 20,000 ADT cycles at RT.

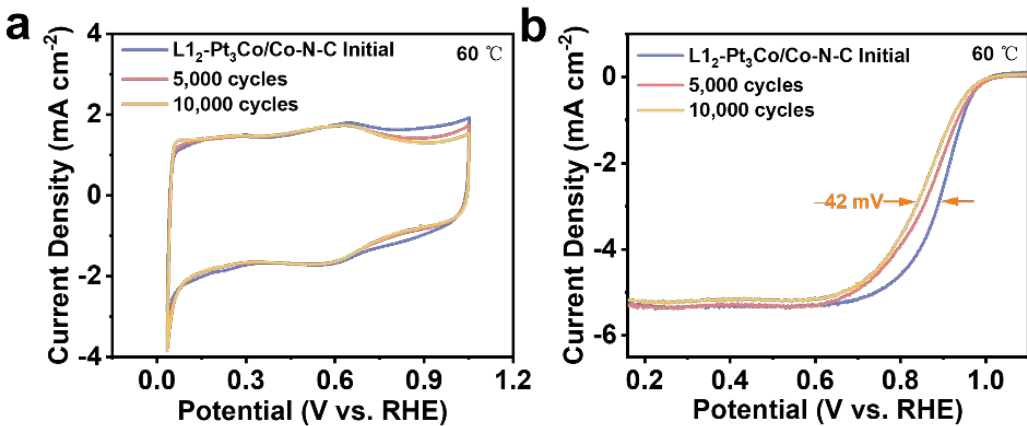


Figure S32. (a) CV curves of $\text{L1}_2\text{-Pt}_3\text{Co/Co-N-C}$ in N_2 -saturated 0.1 M HClO_4 before and after ADT at 60°C . (b) ORR polarization curves of $\text{L1}_2\text{-Pt}_3\text{Co/Co-N-C}$ in O_2 -saturated 0.1 M HClO_4 before and after ADT at 60°C .

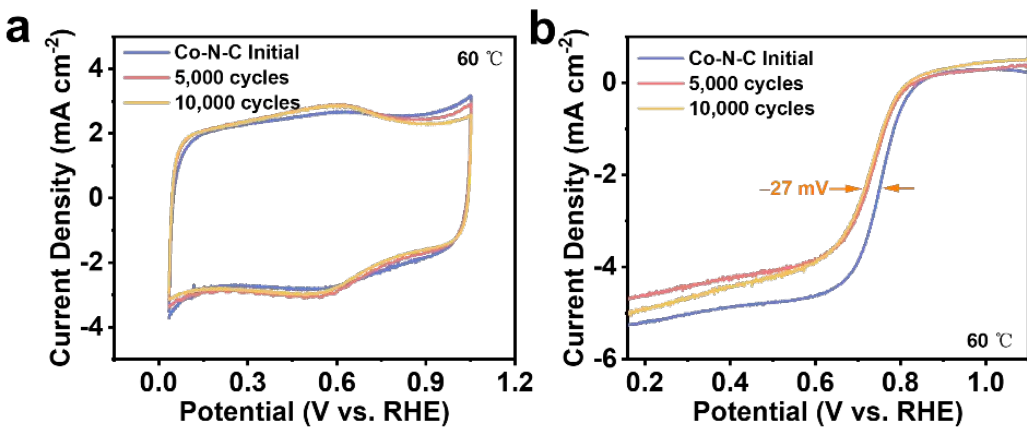


Figure S33. (a) CV curves of Co-N-C in N_2 -saturated 0.1 M HClO_4 before and after ADT at 60°C . (b) ORR polarization curves of Co-N-C in O_2 -saturated 0.1 M HClO_4 before and after ADT at 60°C .

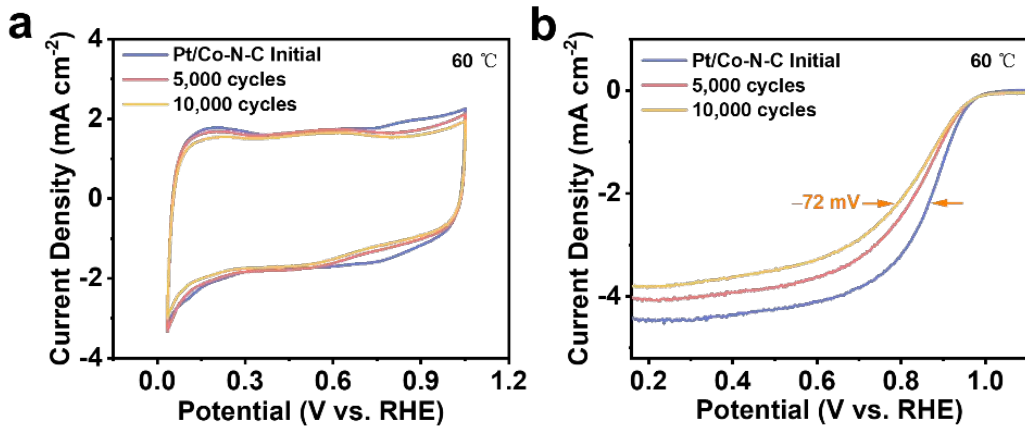


Figure S34 (a) CV curves of Pt/Co-N-C in N_2 -saturated 0.1 M HClO_4 before and after ADT at 60 °C. (b) ORR polarization curves of Pt/Co-N-C in O_2 -saturated 0.1 M HClO_4 before and after ADT at 60 °C.

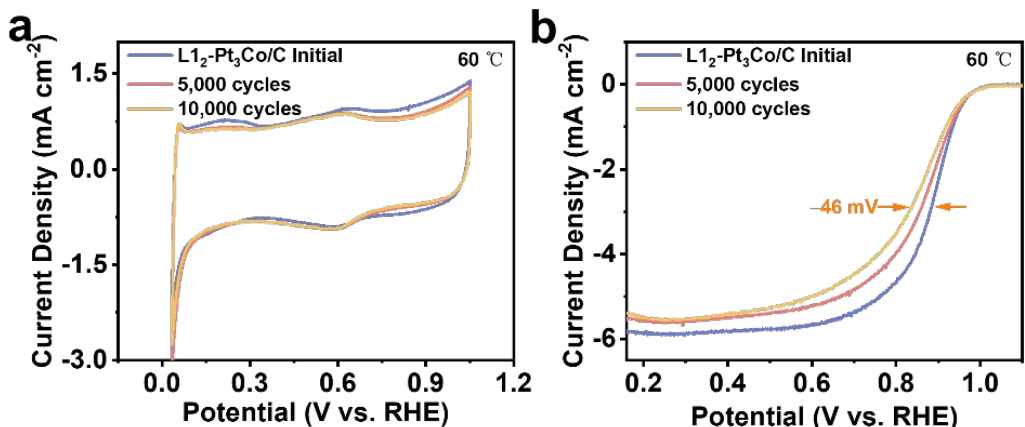


Figure S35. (a) CV curves of L₁₂-Pt₃Co/C in N_2 -saturated 0.1 M HClO_4 before and after ADT at 60 °C. (b) ORR polarization curves of L₁₂-Pt₃Co/C in O_2 -saturated 0.1 M HClO_4 before and after ADT at 60 °C.

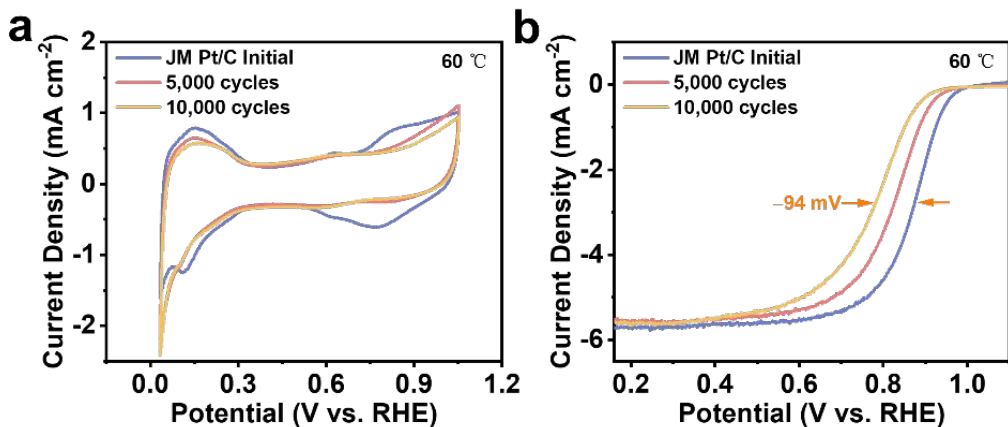


Figure S36. (a) CV curves of JM Pt/C in N_2 -saturated 0.1 M HClO_4 before and after ADT at 60 °C. (b) ORR polarization curves of JM Pt/C in O_2 -saturated 0.1 M HClO_4 before and after ADT at 60 °C.

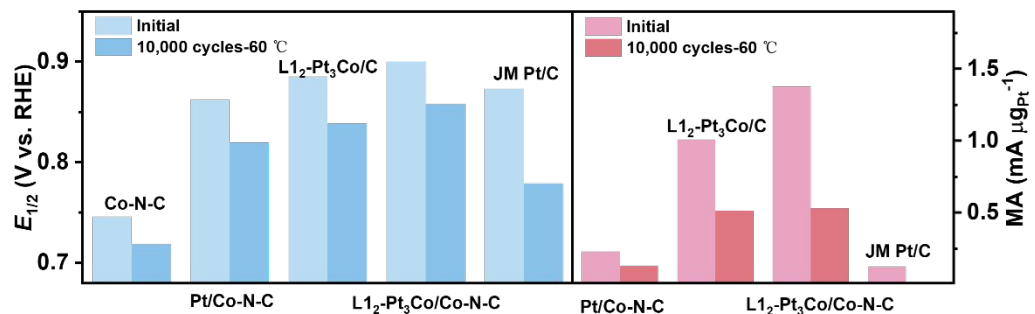


Figure S37. $E_{1/2}$, MA (@0.9 V), and SA (@0.9 V) values for the studied catalysts before and after 10,000 ADT cycles at 60 °C.

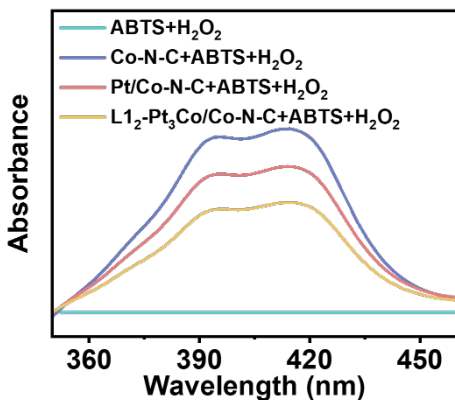


Figure S38. UV-vis absorption spectra of Co-N-C, Pt/Co-N-C, and L₁₂-Pt₃Co/Co-N-C in 0.1 M HClO₄ electrolyte containing ABTS+H₂O₂ solution.

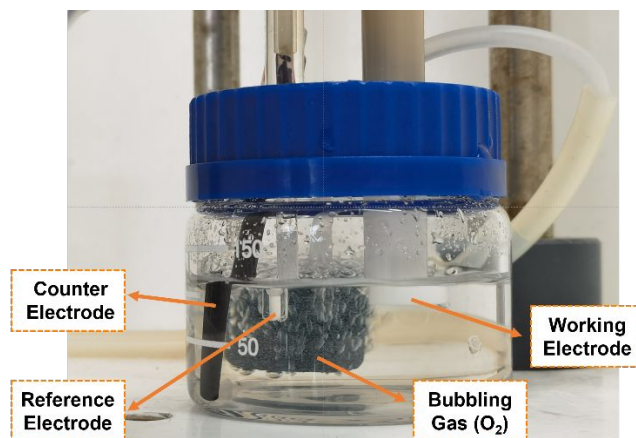


Figure S39. A simple electrochemical cell for collected a constant volume of electrolyte for ICP-MS during ADT.

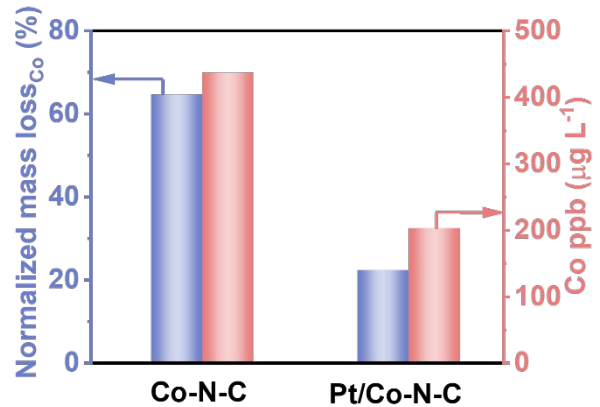


Figure S40. The relative amount of Co sites loss obtained from the mapping and the amount of Co ions dissolved in the electrolyte obtained from ICP-MS for Co-N-C and Pt/Co-N-C catalyst after 10,000 ADT cycles at RT.

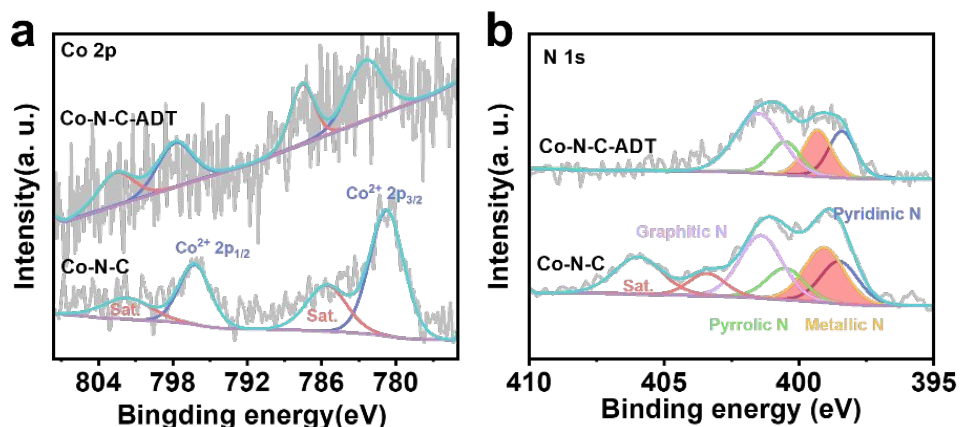


Figure R41. (a) Co 2p XPS spectra and (b) N 1s XPS spectra of Co-N-C before and after ADT at RT.

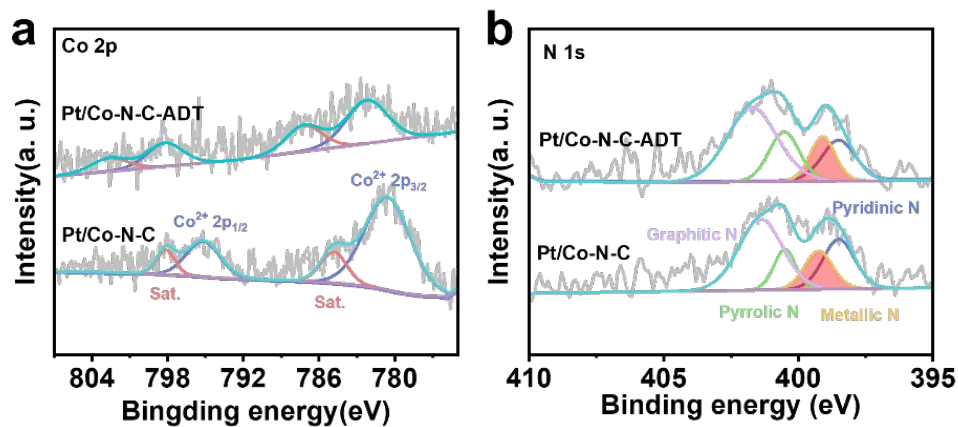


Figure R42. (a) Co 2p XPS spectra and (b) N 1s XPS spectra of Pt/Co-N-C before and after ADT at RT.

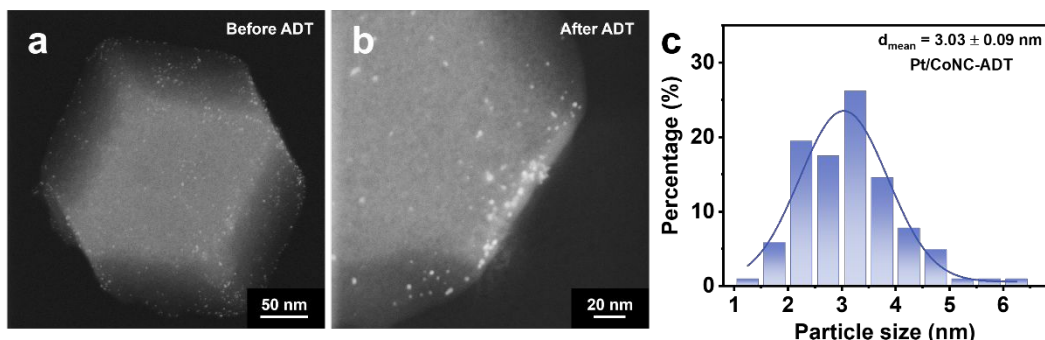


Figure S43. (a, b) HAADF-STEM images of Pt/Co-N-C and (c, d) HAADF-STEM images of L1₂-Pt₃Co/Co-N-C after 10,000 ADT cycles at RT.

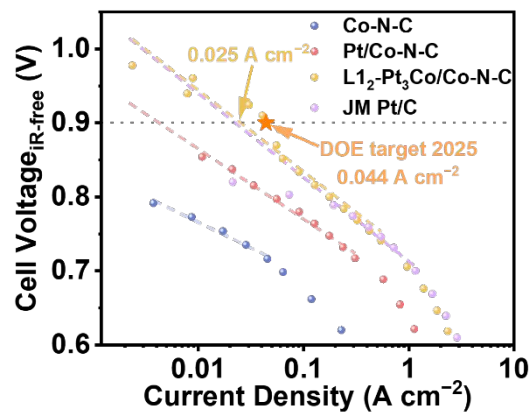
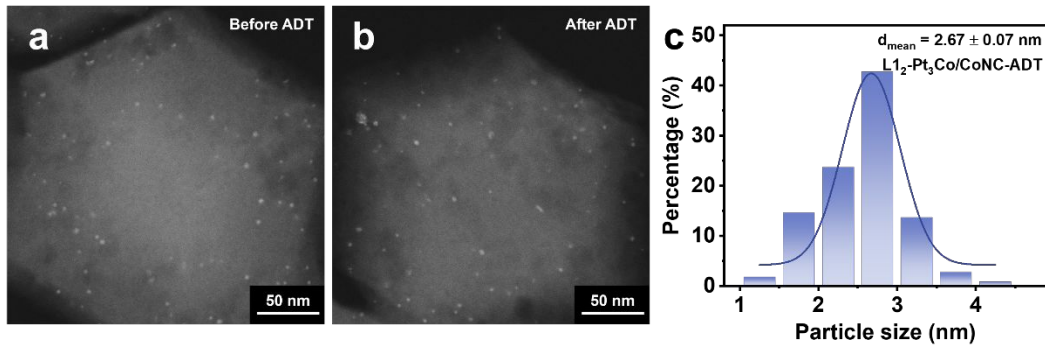


Figure S45. MA of the catalysts at 0.9 V_{iR-free} under a back pressure of 150 kPa abs. The orange star denotes the US DOE target for 2025.

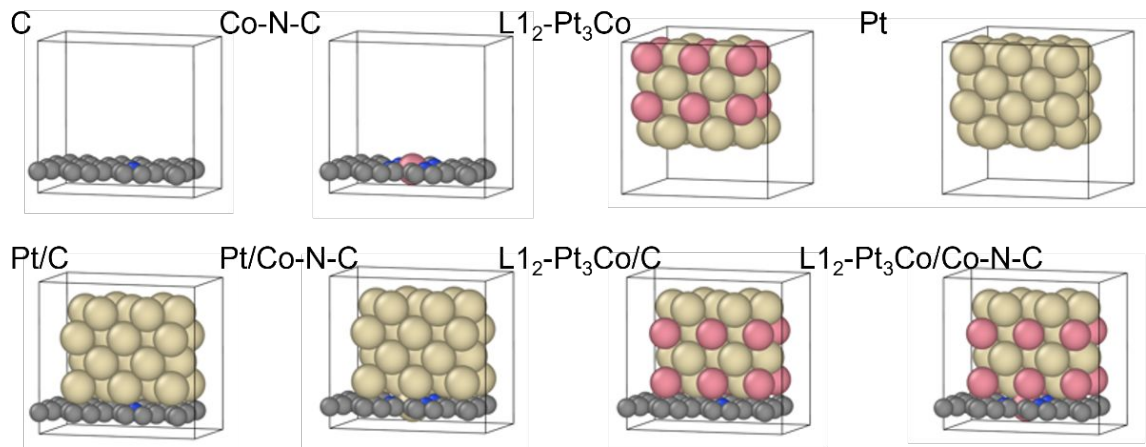


Figure S46. Structures to generate MLP.

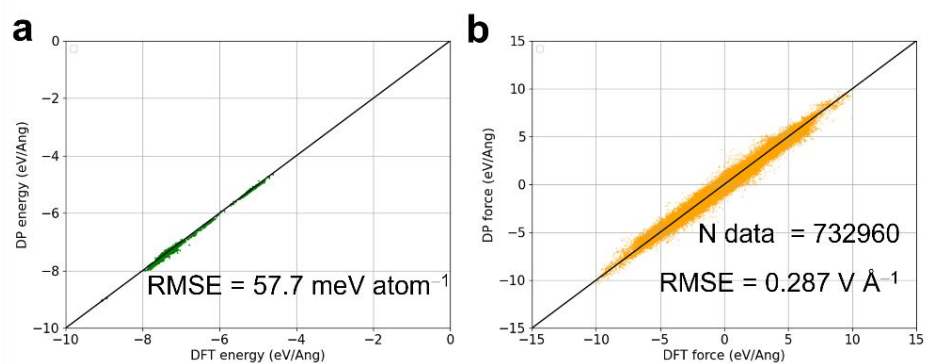


Figure S47. The comparison between the DP and DFT energy and forces.

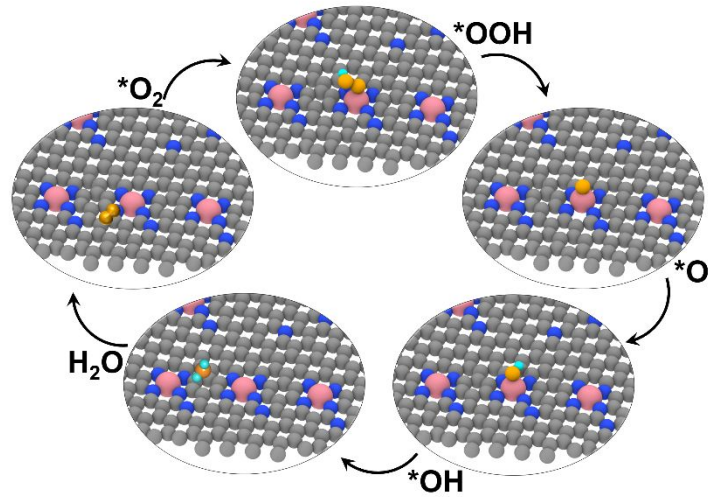


Figure S48. Schematic ORR pathway on Co-N_4 site in Co-N-C .

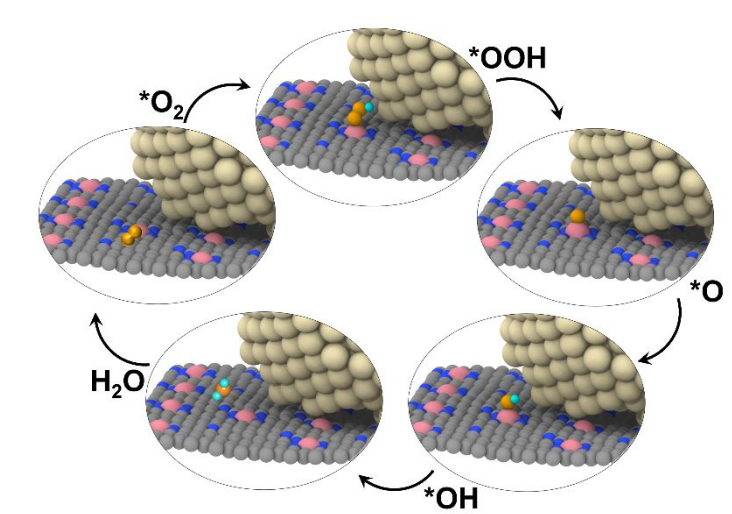


Figure S49. Schematic ORR pathway on Co-N_4 site adjacent to the Pt NPs in Pt/Co-N-C .

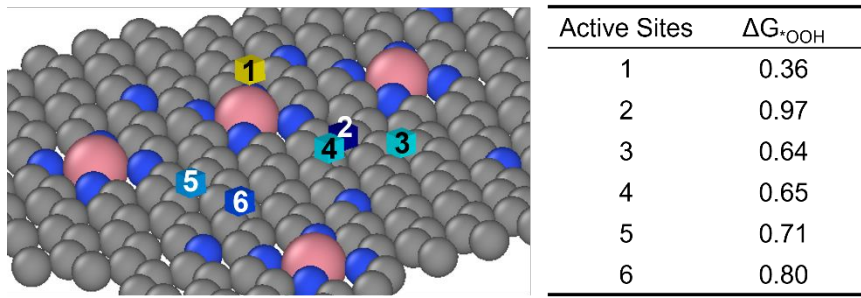


Figure S50. Multiple active sites and their corresponding $\text{O}_2 \rightarrow \text{*OOH}$ reaction energy barriers in Co-N-C model.

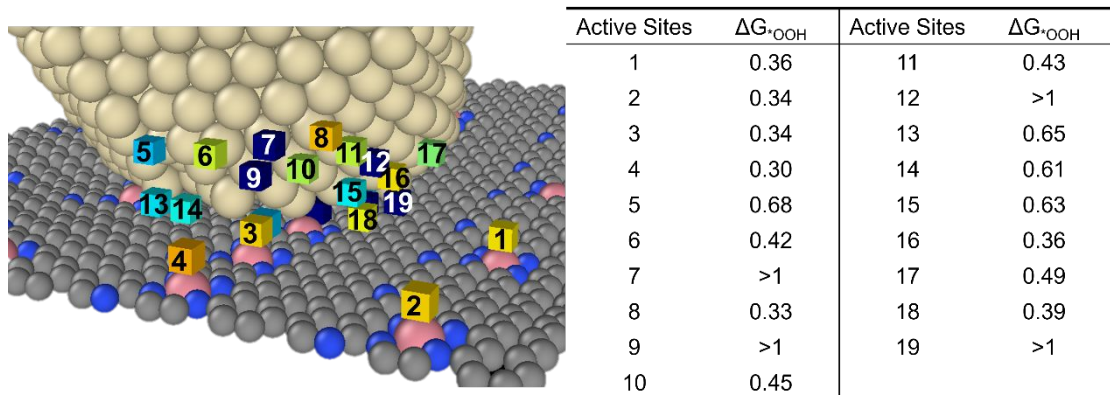


Figure S51. Multiple active sites and their corresponding $\text{O}_2 \rightarrow \text{*OOH}$ reaction energy barriers in Pt/Co-N-C model.

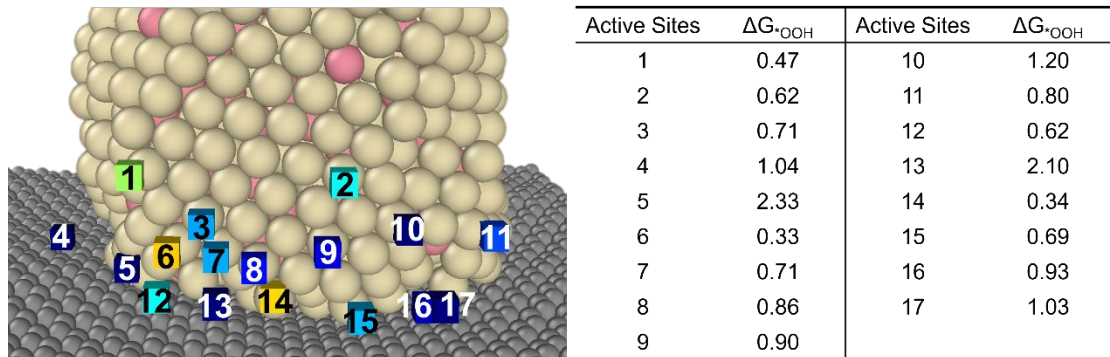


Figure S52. Multiple active sites and their corresponding $\text{O}_2 \rightarrow \cdot\text{OOH}$ reaction energy barriers in $\text{L1}_2\text{-Pt}_3\text{Co/C}$ model.

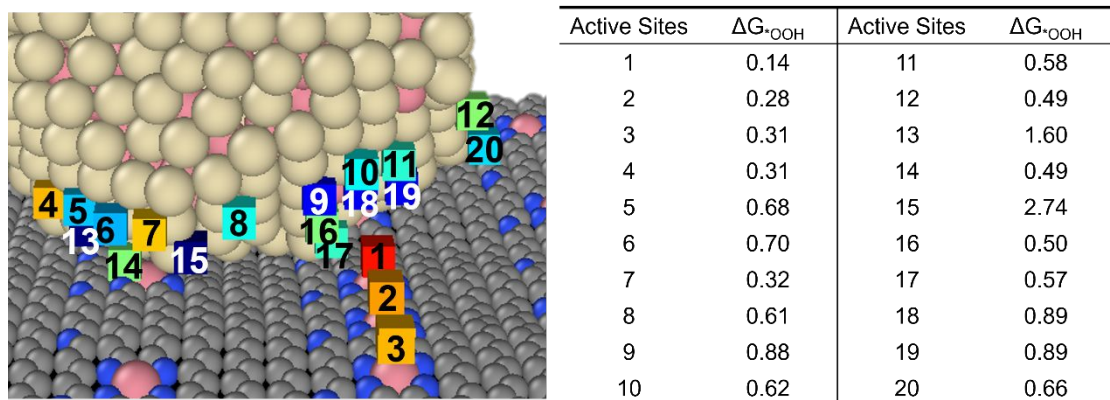


Figure S53. Multiple active sites and their corresponding $\text{O}_2 \rightarrow \cdot\text{OOH}$ reaction energy barriers in $\text{L1}_2\text{-Pt}_3\text{Co/Co-N-C}$ model.

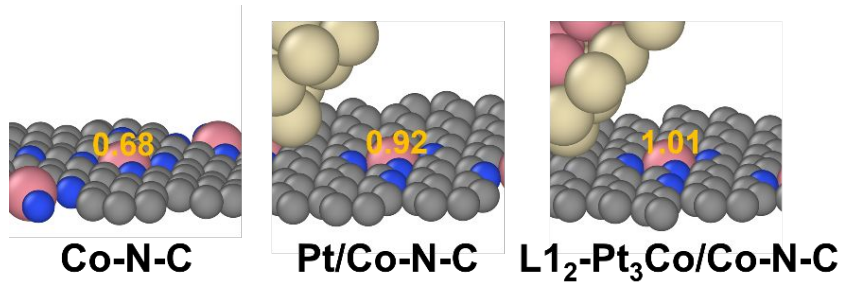


Figure S54. The spin density of Co within Co-N₄ site for Co-N-C, Pt/Co-N-C, and L1₂-Pt₃Co/Co-N-C.

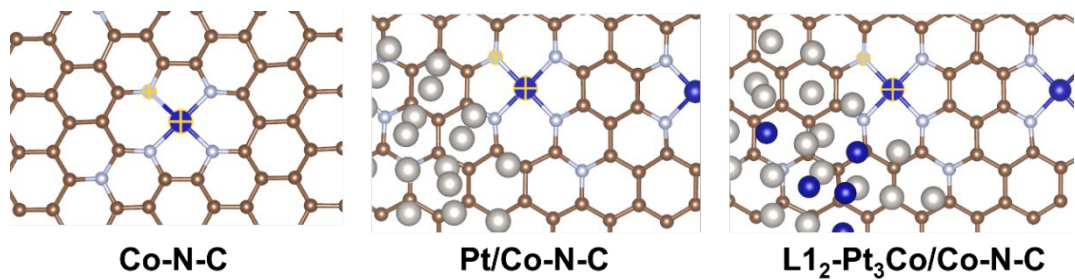


Figure S55. The models of Co-N bond for Co-N-C, Pt/Co-N-C, and L1₂-Pt₃Co/Co-N-C.

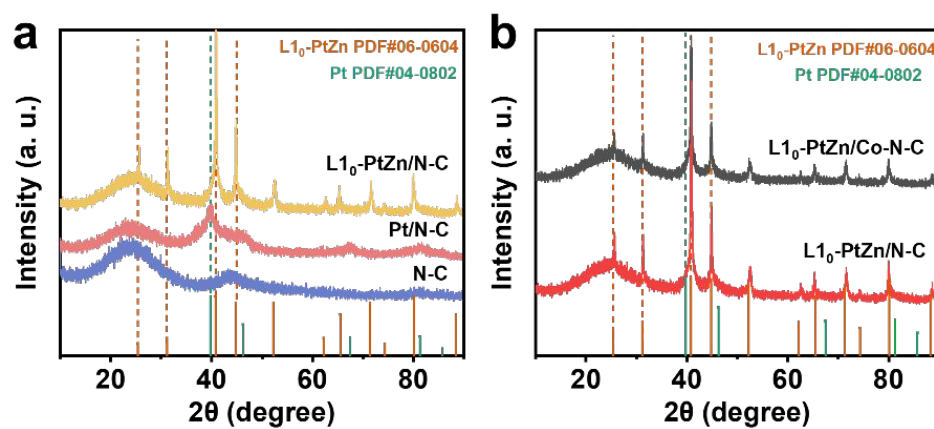


Figure S56. (a) XRD patterns of N-C, Pt/N-C, and L1₀-PtZn/N-C. (b) XRD patterns of L1₀-PtZn/N-C and L1₀-PtZn/Co-N-C.

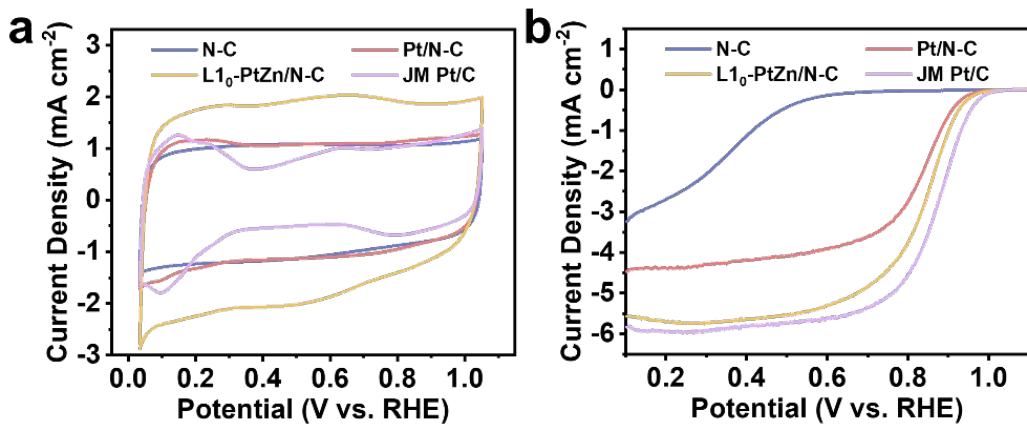


Figure S57. (a) CV curves of N-C, Pt/N-C, L1₀-PtZn/N-C, and JM Pt/C in N_2 -saturated 0.1 M HClO_4 with a scanning rate of 50 mV s⁻¹. Loading: 100 $\mu\text{g}_{\text{catalyst}} \text{cm}^{-2}$ of JM Pt/C catalyst and 200 $\mu\text{g}_{\text{catalyst}} \text{cm}^{-2}$ of other catalysts. (b) ORR polarization curves of N-C, Pt/N-C, L1₀-PtZn/N-C, and JM Pt/C in O_2 -saturated 0.1 M HClO_4 with a scanning rate of 10 mV s⁻¹ and rotation rate of 1600 rpm.

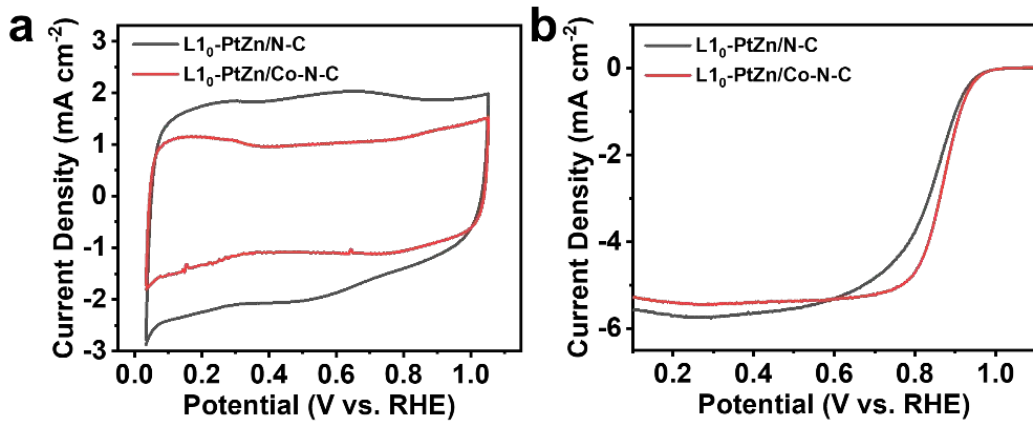


Figure S58. (a) CV curves and (b) ORR polarization curves of L1₀-PtZn/N-C and L1₀-PtZn/Co-N-C.

5. Supplementary Tables

Table S1. ICP-OES results of L₁₂-Pt₃Co/Co-N-C before and after acid washing.

Sample	Co (wt%)	Pt (wt%)
L ₁₂ -Pt ₃ Co/Co-N-C (Before acid washing)	44.9583	3.8131
L ₁₂ -Pt ₃ Co/Co-N-C (After acid washing)	1.4686	1.6907

Table S2. ICP-OES results for the prepared samples.

Sample	Co (wt%)	Pt (wt%)
Co-N-C	1.8223	-
Pt/Co-N-C	1.1284	4.4493
L ₁₂ -Pt ₃ Co/Co-N-C	1.4686	1.6907

Table S3. The relative content of N elements and Co-N_x coordination on the surface of the prepared samples measured by XPS

Sample	N (at%)	Co-N _x (at%)
Co-N-C	3.02	0.65
Pt/Co-N-C	3.67	0.55
L ₁₂ -Pt ₃ Co/Co-N-C	3.09	0.28

Table S4. Structural parameters of Pt foil, Co foil, L1₂-Pt₃Co/Co-N-C, and Pt/Co-N-C extracted from the EXAFS fitting.

Sample	Shell	CN ^a	R(Å) ^b	σ^2 (Å ² ·10 ⁻³) ^c	ΔE_0 (eV) ^d	R factor (%)
Pt foil	Pt-Pt	12*	2.76	0.0044	7.66	0.2
Co foil	Co-Co	12*	2.49	0.0060	7.26	0.2
L1 ₂ - Pt ₃ Co/ Co-N-C	Pt-Co	5.1	2.63	0.0091	7.90	1.2
	Pt-Pt	5.7	2.66	0.0063	-0.32	
Pt/Co-N- C	Co-N	3.7	1.98	0.0136	-9.90	1.1
	Pt-Pt	5.5	2.74	0.0048	4.41	1.2
C	Co-N	4.0	1.94	0.0030	0.43	0.9

CN^a: coordination numbers; *R*^b: bond distance; σ^2 ^c: Debye-Waller factors to account for both thermal and structural disorders; ΔE_0 ^d: the inner potential correction. *R* factor: goodness of fit. S_0^2 was set as 0.81 for Pt data, and 0.73 for Co data. which was obtained from the experimental EXAFS fit of mental foil reference by fixing CN as the known crystallographic value and was fixed to all the samples.

Table S5. $E_{1/2}$ and MA of catalysts before and after ADT at RT.

Sample	Initial- $E_{1/2}$ (V)	1w- $E_{1/2}$ (V)	Initial-MA (mA $\mu\text{g}_{\text{Pt}}^{-1}$)	1w-MA (mA $\mu\text{g}_{\text{Pt}}^{-1}$)
Co-N-C	0.745	0.695	-	-

Pt/Co-N-C	0.839	0.819	0.122	0.082
L1 ₂ -Pt ₃ Co/C	0.861	0.777	0.620	0.172
L1 ₂ -Pt ₃ Co/Co-N-C	0.895	0.931	1.385	3.487
JM Pt/C	0.862	0.802	0.105	0.040

Table S6. $E_{1/2}$ and MA of catalysts before and after ADT at 60 °C.

Sample	Initial- $E_{1/2}$ (V)	1w- $E_{1/2}$ (V)	Initial-MA (mA $\mu\text{g}_{\text{Pt}}^{-1}$)	1w-MA (mA $\mu\text{g}_{\text{Pt}}^{-1}$)
Co-N-C	0.746	0.719	-	-
Pt/Co-N-C	0.862	0.820	0.230	0.128
L1 ₂ -Pt ₃ Co/C	0.885	0.839	1.007	0.515
L1 ₂ -Pt ₃ Co/Co-N-C	0.900	0.858	1.377	0.534
JM Pt/C	0.873	0.779	0.124	0.015

Table S7. Comparison of RDE ORR performance of L1₂-Pt₃Co/Co-N-C with several advanced catalysts from recent published works.

Sample	Catalyst loading (mg cm ⁻²)	Pt loading ($\mu\text{g}_{\text{Pt}} \text{cm}^{-2}$)	$E_{1/2}$ (V)	MA@0.9 V _{iR-free} (A mg _{Pt} ⁻¹)	Durability	Electrolyte	Reference
L1 ₂ -Pt ₃ Co/Co-N-C	0.2	3.4	0.895	1.385	MA=1.60 A mg _{Pt} ⁻¹ after 80,000 cycles 32.8% MA loss after 20,000 cycles	0.1 M HClO ₄	This work
Pt/Co-N-C	0.2	8.9	0.839	0.122	50 mV $E_{1/2}$ loss after 20,000 cycles	0.1 M HClO ₄	This work
Co-N-C	0.2	N/A	0.745	N/A	61.9% MA loss after 20,000 cycles	0.1 M HClO ₄	This work
JM Pt/C	0.1	20	0.862	0.105	14 mV $E_{1/2}$ loss after 40,000	0.1 M HClO ₄	This work
Pt-Fe-N-C	0.25	4.25	0.909	N/A	[8]		

						cycles	HClO ₄	
LP@PF-1	N/A	3.0	0.941	8.64		N/A	0.1 M HClO ₄	[9]
LP@PF-2	N/A	3.2	0.959	12.36		N/A	0.1 M HClO ₄	[9]
L1 ₂ -Pt ₃ Co@Mn _{SA-} NC	N/A	20	0.965	1.8	10 mV $E_{1/2}$ loss after 30,000 cycles	0.1 M HClO ₄	[10]	
Pt@Mn _{SA} -NC	N/A	20	0.915	0.45	1 mV $E_{1/2}$ loss after 30,000 cycles	0.1 M HClO ₄	[10]	
fct-PtCo@Co-N-C	0.128	15.94	0.95	1.96	9.2% MA loss after 20,000 cycles	0.1 M HClO ₄	[11]	
Pt ₃ Ni@Ni-N ₄ -C	0.25	11.75	0.93	1.92	2.1% MA loss after 30,000 cycles	0.1 M HClO ₄	[12]	
Fe _{SA} /Fe _{AC} -2DNPC	0.4	N/A	0.81	N/A	15 mV $E_{1/2}$ loss after 10,000	0.5 M	[13]	

					cycles	H ₂ SO ₄	
Fe-N-C	0.6	N/A	0.93	N/A	100 mV $E_{1/2}$ loss after 30,000 cycles	0.5 M H ₂ SO ₄	[14]
Co(mIm)-NC(1.0)	0.6	N/A	0.82	N/A	8 mV $E_{1/2}$ loss after 10,000 cycles	0.5 M H ₂ SO ₄	[15]
Fe(mIm)-NC(1.0)	0.6	N/A	0.84	N/A	28 mV $E_{1/2}$ loss after 30,000 cycles	0.5 M H ₂ SO ₄	[15]

Table S8. The values of ZPE and TS (units: eV). Those values are taken from Ref[4].

Species	ZPE	TS
OOH	0.37	0
O*	0.072	0.038
OH*	0.4	0

REFERENCES

1. Behler, J.; Parrinello, M. Generalized Neural-Network Representation of High-Dimensional Potential-Energy Surfaces. *Phys. Rev. Lett.* **2007**, *98*, 146401.
2. Zhang, Y.; Wang, H.; Chen, W.; Zeng, J.; Zhang, L.; Wang, H.; E, W. DP-GEN: A Concurrent Learning Platform for the Generation of Reliable Deep Learning Based Potential Energy Models. *Comput. Phys. Commun.* **2020**, *253*, 107206.
3. Thompson, A. P.; Aktulga, H. M.; Berger, R.; Bolintineanu, D. S.; Brown, W. M.; Crozier, P. S.; in't Veld, P. J.; Kohlmeyer, A.; Moore, S. G.; Nguyen, T. D. LAMMPS—A Flexible Simulation Tool for Particle-Based Materials Modeling at the Atomic, Meso, and Continuum Scales. *Comput. Phys. Commun.* **2022**, *271*, 108171.
4. Siti, Z. M.; Joanita, S.; Khairun Nisa, J.; Balkish, M. N.; Tahir, A. Pacifier Use and its Association with Breastfeeding and Acute Respiratory Infection (ARI) in Children Below 2 Years Old. *Med. J. Malays.* **2013**, *68*, 125—128.
5. Grimme, S.; Antony, J.; Ehrlich, S.; Krieg, H. A Consistent and Accurate Ab Initio Parametrization of Density Functional Dispersion Correction (DFT-D) for the 94 Elements H-Pu. *J. Chem. Phys.* **2010**, *132*, 154104.

6. Giannozzi, P.; Baroni, S.; Bonini, N.; Calandra, M.; Car, R.; Cavazzoni, C.; Ceresoli, D.; Chiarotti, G. L.; Cococcioni, M.; Dabo, I.; Dal Corso, A.; de Gironcoli, S.; Fabris, S.; Fratesi, G.; Gebauer, R.; Gerstmann, U.; Gougaussis, C.; Kokalj, A.; Lazzeri, M.; Martin-Samos, L.; Marzari, N.; Mauri, F.; Mazzarello, R.; Paolini, S.; Pasquarello, A.; Paulatto, L.; Sbraccia, C.; Scandolo, S.; Sclauzero, G.; Seitsonen, A. P.; Smogunov, A.; Umari, P.; Wentzcovitch, R. M. QUANTUM ESPRESSO: A Modular and Open-Source Software Project for Quantum Simulations of Materials. *J. Phys.: Condens. Matter* **2009**, *21*, 395502.

7. Wang, H.; Zhang, L.; Han, J.; E, W. DeePMD-Kit: A Deep Learning Package for Many-Body Potential Energy Representation and Molecular Dynamics. *Comput. Phys. Commun.* **2018**, *228*, 178—184.

8. Xiao, F.; Wang, Q.; Xu, G.; Qin, X.; Hwang, I.; Sun, C.; Liu, M.; Hua, W.; Wu, H.-W.; Zhu, S.; Li, J.; Wang, J.; Zhu, Y.; Wu, D.; Wei, Z.; Gu, M.; Amine, K.; Shao, M. Atomically Dispersed Pt and Fe Sites and Pt-Fe Nanoparticles for Durable Proton Exchange Membrane Fuel Cells. *Nat. Cata.* **2022**, *5*, 503—512.

9. Chong, L.; Wen, J. G.; Kubal, J.; Sen, F. G.; Zou, J. X.; Greeley, J.; Chan, M.; Barkholtz, H.; Ding, W. J.; Liu, D. J. Ultralow-Loading Platinum-Cobalt Fuel Cell Catalysts Derived from Imidazolate Frameworks. *Science* **2018**, *362*, 1276—1281.

10. Zeng, Y.; Liang, J.; Li, C.; Qiao, Z.; Li, B.; Hwang, S.; Kariuki, N. N.; Chang, C.; Wang, M.; Lyons, M.; Lee, S.; Feng, Z.; Wang, G.; Xie, J.; Cullen, D. A.; Myers, D. J.; Wu, G. Regulating Catalytic Properties and Thermal Stability of Pt and PtCo Intermetallic Fuel-Cell Catalysts via Strong Coupling Effects between Single-Metal Site-Rich Carbon and Pt. *J. Am. Chem. Soc.* **2023**, *145*, 17643—17655.
11. Chen, J.; Dong, J.; Huo, J.; Li, C.; Du, L.; Cui, Z.; Liao, S. Ultrathin Co-N-C Layer Modified Pt–Co Intermetallic Nanoparticles Leading to a High-Performance Electrocatalyst toward Oxygen Reduction and Methanol Oxidation. *Small* **2023**, *19*, 2301337.
12. Yan, W.; Guo, O.; Xing, Q.; Liao, M.; Shi, Z.; Feng, H.; Zhang, Y.; Li, X.; Chen, Y. Atomically Dispersed Ni–N₄ Sites Assist Pt₃Ni Nanocages with Pt Skin to Synergistically Enhance Oxygen Reduction Activity and Stability. *Small* **2023**, *19*, 202300200.
13. Wan, X.; Liu, Q.; Liu, J.; Liu, S.; Liu, X.; Zheng, L.; Shang, J.; Yu, R.; Shui, J. Iron Atom-Cluster Interactions Increase Activity and Improve Durability in Fe–N–C Fuel Cells. *Nat. Commun.* **2022**, *13*, 2963.
14. Zeng, Y.; Li, C.; Li, B.; Liang, J.; Zachman, M. J.; Cullen, D. A.; Hermann, R. P.; Alp, E. E.; Lavina, B.; Karakalos, S.; Lucero, M.; Zhang, B.; Wang, M.; Feng,

Z.; Wang, G.; Xie, J.; Myers, D. J.; Dodelet, J.-P.; Wu, G. Tuning the Thermal Activation Atmosphere Breaks the Activity–Stability Trade-Off of Fe–N–C Oxygen Reduction Fuel Cell Catalysts. *Nat. Cata.* **2023**, *6*, 1215–1227.

15. Xie, X.; He, C.; Li, B.; He, Y.; Cullen, D. A.; Wegener, E. C.; Kropf, A. J.; Martinez, U.; Cheng, Y.; Engelhard, M. H.; Bowden, M. E.; Song, M.; Lemmon, T.; Li, X. S.; Nie, Z.; Liu, J.; Myers, D. J.; Zelenay, P.; Wang, G.; Wu, G.; Ramani, V.; Shao, Y. Performance Enhancement and Degradation Mechanism Identification of a Single-Atom Co–N–C Catalyst for Proton Exchange Membrane Fuel Cells. *Nat. Cata.* **2020**, *3*, 1044–1054.